Coordinated satellite, aircraft, and ground-based observations of a large transient methane release

Tai-Long He[1], Daniel J. Varon[1,2], Shobha Kondragunta[3], Xinrong Ren[4], Mark D. Cohen[4], Brian J. Carroll[5,6], Nathan Malarich[5,6], Jeffrey Peischl[5,7], Tobias A. de Jong[8], Jelmar Gerritsen[8], Joannes D. Maasakkers[8], Daniel H. Cusworth[9], Riley M. Duren[9], Steven S. Brown[6], Carsten Warneke[6], Colm Sweeney[7], Phillip Stratton[4,10], Alan Brewer[6], Sunil Baidar[5,6], Ezra J. T. Levin[11]

[1]Institute for Data, Systems, and Society, Massachusetts Institute of Technology, [2]Department of Aeronautics and Astronautics, Massachusetts Institute of Technology, [3]NOAA/NESDIS, [4]NOAA Air Resources Laboratory, [5]Cooperative Institute for Research in Environmental Sciences (CIRES), University of Colorado Boulder, [6]NOAA Chemical Sciences Laboratory, [7]NOAA Global Monitoring Laboratory, [8]Space Research Organisation Netherlands (SRON), [9]Carbon Mapper, Inc, [10]Department of Atmospheric and Oceanic Science / Cooperative Institute for Satellite Earth System Studies (CISESS), University of Maryland, [11]Energy Institute, Colorado State University, [12]Department of Systems Engineering, Colorado State University.

*Tai-Long He, Daniel J. Varon.

Email: tlhe@mit.edu, dvaron@mit.edu

January 2026

Abstract

We present results from a Very Large Methane Release (VLMR) experiment evaluating methane retrievals from the Geostationary Operational Environmental Satellites (GOES) Advanced Baseline Imagers (ABIs) and multiple low-Earth-orbit imagers with high point-source detection limits. The experiment coordinated observations of a U.S. gas pipeline blowdown with nine satellites, two aircraft, and a truck-based mobile laboratory. We used the GOES-16, -18, and -19 ABIs with revisits every 10 min to 7 s to quantify release magnitude and uncertainty. Best methane retrieval precision (7–8%) was achieved in the 7-s and 30-s mesoscale scan modes averaged to 5 min. Source-rate and mass estimates are broadly consistent across measurement platforms. Detectable emissions totaled 370±30 t over 44–65 min from two release points, ~25% lower than bottom-up expectations based on pipeline volume and nominal pressure, likely due to late-stage emissions below satellite detection limits. Our work provides a framework for evaluating high-detection-limit methane point-source imagers.

Significance Statement

Methane is a potent greenhouse gas, and emissions from oil and gas infrastructure are a major mitigation target. Satellites are increasingly used to detect and quantify these emissions, but evaluating their estimates of releases remains challenging. In this study, we analyze a U.S. gas pipeline blowdown in New Mexico using coordinated observations from nine satellites, two aircraft, and a truck-based mobile laboratory. Our experiment provides a rare opportunity to evaluate the accuracy of satellite-based observations of large, short-lived methane point sources. We show that geostationary satellites can continuously track and quantify such releases, with emission estimates consistent with other platforms and expectations from pipeline pressure and volume. Our results build confidence in satellite observations to monitor extreme methane releases worldwide.

Introduction

Satellite capabilities for monitoring atmospheric methane point sources are advancing rapidly. A growing constellation of instruments in low-Earth orbit (LEO) and geostationary orbit (GEO) can detect and quantify individual point sources worldwide with high resolution and revisit rates (Jacob et al., 2022; Mohammadimanesh et al., 2025). Dedicated point-source imagers such as GHGSat and Carbon Mapper offer high pixel resolution (~30 m) and low plume detection limits (~100 kg h^{-1}) for targeted regions of order 10×10 km^2 (Jervis et al., 2021; Duren et al., 2025); wide-swath pushbroom spectrometers including the TROPOspheric Monitoring Instrument (TROPOMI; Schuit et al., 2023) and multispectral imagers such as the Visible Infrared Imaging Radiometer Suite (VIIRS; de Jong et al., 2025) provide routine global coverage for large point sources; and GEO instruments including the Geostationary Operational Environmental Satellites (GOES) Advanced Baseline Imager (ABI) offer continuous hemispheric scans every few minutes with sensitivity to the largest transient methane releases (Watine-Guiu et al., 2023; Zhou et al., 2025).

Previous studies have evaluated satellite point-source detection limits based on plume population statistics (e.g., Lauvaux et al., 2022; Schuit et al., 2023; Ayasse et al., 2024) or synthetic plume data (e.g., Cusworth et al., 2019; Gorrono et al., 2023). More recently, detection limits and source-rate estimates have been assessed by controlled release (Sherwin et al., 2023; Worden et al., 2025). Controlled-release experiments are increasingly common but have so far been limited to source rates <10 t h^{-1} due to cost and safety constraints, and ongoing experiments simulate sources <3 t h^{-1} (Sherwin et al., 2024). These experiments provide valuable benchmarks for instruments with detection thresholds of ~1 t h^{-1} or less, but are not applicable to wide-swath sensors with higher detection limits (>10 t h^{-1}) such as TROPOMI, VIIRS, and GOES ABI.

Here we present the results of a Very Large Methane Release (VLMR) experiment evaluating the ability of such instruments to detect and quantify emissions, with a focus on GOES ABI. The experiment was conducted on 8 October 2024 in New Mexico, U.S. and involved coordinated observations of a planned gas pipeline blowdown event by a suite of ground, aerial, and satellite instruments as depicted in Figure 1. We quantify the resulting emissions using three GOES ABIs (GOES-16, GOES-18, and GOES-19); six LEO instruments including TROPOMI, the Visible Infrared Imaging Radiometer Suite (VIIRS) on the Suomi-NPP, NOAA-20, and NOAA-21 satellites; the Sea and Land Surface Temperature Radiometer (SLSTR) on Sentinel-3; and the Ocean Colour Instrument (OCI) on PACE; two aerial platforms including the NASA Airborne Visible/Infrared Imaging Spectrometer-3 (AVIRIS-3) and NOAA/ChampionX Mooney aircraft; and the NOAA Pick-Up Based Mobile Atmospheric Sounder (PUMAS) mobile laboratory. The GOES ABI observations from three vantage points in GEO provide measurement frequencies of 10 min down to 7 s, allowing estimation of time-dependent plume mass, emission rate, and associated uncertainties. The LEO instruments provide additional snapshots of the release plumes, and the aircraft and ground-based platforms provide detailed information on the release duration, local meteorology, and in-situ methane concentrations as well as estimates of release rates. Estimates of total plume mass and source rate are compared between measurement platforms and evaluated against bottom-up estimates based on pipeline pressure and volume as described by the pipeline operators.

Results and Discussion

Figure 2 shows the AVIRIS-3, Mooney, and PUMAS methane measurements taken over the course of the experiment. The pipeline blowdown was initially scheduled for 14:00 UTC (9:00 am LT) but was delayed several hours. It ultimately began at 17:25 UTC at the western site and 17:36 UTC at the eastern site (±1 min, as observed by the aerial and ground teams). AVIRIS-3 was diverted from a nearby research flight track and captured methane enhancements from a test release at 16:13 UTC prior to blowdown at the eastern release site. Figure 2B shows the test-release plume with a total estimated methane mass of 495 kg.

The Mooney aircraft entered the experimental region at 16:20 UTC and flew to the western release site, where it remained in a holding pattern until the releases began. From 17:29 to 17:52 UTC, it performed two 1-km-radius spiral profiles around the western source at altitudes of 100–600 m agl (Figure 2C). Peak methane concentrations of 226 ppm were observed from the western source at 17:45 UTC. The aircraft then obtained two spiral profiles over the eastern site from 18:06 to 18:28 UTC (Figure 2D; 130–355 m agl). Finally, it returned to the western release point and performed three in-plume spirals to determine the boundary layer depth, followed by two cross-plume transects at 375 m and 510 m agl ~25 km downwind. The aircraft measurements concluded around 19:45 UTC.

The PUMAS truck measured a peak 1-s-average concentration of 289 ppm 1.85 km downwind of the eastern source at 17:46, about 10 minutes after the blowdown began (Figure 2E). It then drove north to 8.45 km downwind of the eastern source, waited for the plume to arrive, and carried out a ~4 km west-to-east transect roughly perpendicular to the wind direction from 18:20:29 to 18:33:31, during which a peak 1-min-average enhancement of 63 ppm was measured. This transect did not include the entire width of the plume and so was not used for an emission estimate. An east-to-west transect was then carried out from 18:35:30 to 18:45:29 in which a peak 1-min-average methane enhancement of 10.1 ppm was measured. A final west-to-east transect was carried out from 19:08:30 to 19:19:31 and showed a peak 1-min-average enhancement of 0.4 ppm. For these last two transects, the entire width of the plume was measured, and these measurements were used to estimate emission rates from the eastern source by mass balance (Eq. 3 in Materials and Methods).

Figure 3 shows satellite retrievals of methane enhancements from the three GOES and six LEO satellites of Figure 1. Plume signals were first detected in the full-disk and CONUS GOES ABI scans near the western release site in the 17:30 UTC scan, while enhancements over the eastern site were detected in the 17:40 UTC scan. With the higher temporal resolution of the GOES-18 30-s and GOES-19 7-s mesoscale imagery, the initial detections of methane enhancements from the western and eastern releases are more precisely resolved to 17:27 UTC and 17:38 UTC, just 1–2 minutes after the releases began (Figure 3A). The delay is likely due to the time required for the plumes to fill up an ABI image pixel.

Supplemental movie S1 shows animations of the methane plumes derived from GOES ABI. The eastern plume was observed to detach from its source at 18:20 UTC and the western plume at 18:30 UTC, implying detectable blowdown durations of 65 min for the western source (which began 17:25 UTC) and 44 min for the eastern source (which began 17:36 UTC).

We quantify retrieval precision as the standard deviation of background pixels excluding clouds, water, and plumes. Best retrieval precision is achieved in the 30-s and 7-s scan modes averaged to 5 min, with respective mean background standard deviations of 0.044 mol m^{-2} (~7% of 1930-ppb background) and 0.052 mol m^{-2} (~8%). Retrieval precision for the other ABI scan modes is 10%–12%. Sensitivity tests using different averaging windows show that 5-min averaging provides the best balance between noise reduction and plume signal preservation for both 7-s and 30-s scans (see Figures S10, S11).

Figure 3B shows additional snapshots of the releases from the VIIRS, SLSTR, and OCI multispectral LEO instruments with pixel resolutions of 500–1200 m. The first VLMR detection was made by SLSTR aboard Sentinel-3A at 17:35 UTC near the western site. Further downwind detections were captured at ~30–60-min intervals. Retrievals from the LEO sensors show consistent methane enhancements and plume extents. The plumes were also detected by TROPOMI (Figure 3C), with maximum column enhancements of 0.06 mol m^{-2} for the western plume and 0.04 mol m^{-2} for the eastern plume.

Figure 4 compares our observational estimates of methane plume mass and source rate with bottom-up estimates (dashed lines) based on pipeline pressure and volume, and with truck-based and aircraft-based mass balance estimates. Observed total plume mass (Integrated Methane Enhancement, IME; Frankenberg et al., 2016) is computed by summing methane enhancements across plume pixels. Bottom-up estimates based on operator input (dashed lines in Fig. 4) model the releases as sequential exponential decay processes assuming an initial pipeline pressure of 800–950 psi, constant gas temperature of 21.1°C, methane content of 96%, and a 3-hour total release duration (=36 min) to reach atmospheric pressure.

The observed plume mass (Fig. 4A) shows an initial growth phase followed by stabilization as the plumes detach and are advected downwind. This behavior has also been observed by de Jong et al. (2025) with VIIRS and by Zhou et al. (2025) with the Flexible Combined Imager on the Meteosat Third Generation satellite (MTG FCI). Snapshot estimates of plume mass from the GOES ABI and LEO satellite instruments are consistent within uncertainties. GOES ABI infers a total release mass of 370±30 t (Figure 4A; values after 18:45 UTC), with 260±40 t from the western source and 100±50 t from the eastern source. Sentinel-3A/SLSTR observed 100±30 t at 17:35 UTC, during the early growth phase of the western source, compared to 90±20 t for GOES ABI. LEO satellite observations of the detached plumes yield IME values ranging from 350±110 t (VIIRS) to 420±65 t (OCI). TROPOMI quantifies an IME of 360±40 t at 19:33 UTC, within <5% of our nearest GOES ABI estimate. GOES IME uncertainties are estimated from the standard deviation across five data streams, while LEO IME uncertainties are based on the conservative, per-pixel radiance-spread approach of de Jong et al. (2025).

The cumulative plume mass inferred from GOES ABI is consistent with an initial pipeline pressure of approximately 800 psi during the growth phase, but the collection of satellite-based estimates suggests a lower starting pressure during the stabilization phase. Two effects can explain the departure from the 800-psi curve. First, the satellites miss the mass contribution from emissions below their detection limit, which occur later in the release; while they effectively track the initial methane pulse over the first ~45–60 minutes of the blowdown, that mass represents a lower bound on the total amount released. In this case, it underestimates the total expected from the bottom-up isothermal exponential decay model (504 t at 800 psi) by ~25%. Second, the decay model may overestimate release rates later in the blowdown, because it neglects cooling from the Joule-Thompson effect, which can cause icing and hydrate formation at the vent orifice that reduce the effective mass flow rate (API 2020).

Figures 4B–C show estimated instantaneous source rates inferred from GOES ABI as the time derivative of IME for both plumes. The initial growth in source rate (dotted lines in Fig. 4B) likely reflects saturation of methane SWIR absorption lines at the sub-pixel scale early in the release, an effect that would weaken as the plumes diffuse across one or more full pixels. Peak source rates are approximately 500 t h^{-1} for the western source and 360 t h^{-1} for the eastern source. Aircraft spiral measurements for the western source yield source rates 30%–50% lower than concurrent GOES ABI estimates, with 210 ± 30 t h^{-1} at 17:33 UTC followed by a gradual decline to ~140 t h^{-1} and 20 t h^{-1} over ~1 hour. Aircraft and truck-based mass-balance estimates for the eastern source agree with GOES ABI within errors. Discrepancies may be due to incomplete sampling of the turbulent plume, which may not be well-mixed in the near-field of the source, relative to the spatial and temporal resolution of the aircraft spiral measurements. Our GOES ABI source-rate estimates for both release points are consistent with bottom-up estimates based on initial pipeline pressure of 800–950 psi.

Finally, we use GOES ABI's fine temporal sampling to assess its plume detection limit (minimum wind-normalized source rate Q_{min}) for the observing conditions of the experiment. The plumes are first detected at the single-pixel level in the finest-precision 30-s mesoscale scan mode with column enhancements of 0.07–0.08 mol/m^2 over 3.35-km pixels in the 2.25-μm band, reflecting a single-pixel methane mass of ~12 t for initial detection. The steady-state emission rate required to sustain such an enhancement against horizontal transport across the pixel is Q_{min} = 15 t h^{-1} per m s^{-1} of wind, which we take as a lower bound on GOES ABI's detection limit for the VLMR scene. We also estimate Q_{min} using the equation introduced by Jacob et al. (2016):

$$Q_{min} = M_{CH_4} \cdot U \cdot L \cdot q \cdot \sigma \text{ (Eq. 1)}$$

where M_{CH_4} is the molar mass of methane, U is the wind speed, pixel size L=3.35 km, and q is the number of standard deviations above background noise required for single-pixel detection (q=2 by convention). Under 4 m s^{-1} winds (Fig. 3), this yields a minimum detectable source rate of ~110 t h^{-1}, consistent with the uncertainty ranges in Fig. 4B–C. We therefore estimate a detection limit of ~10–30 t h^{-1} per m s^{-1} of wind for GOES ABI for the VLMR experiment scene. This is similar to the detection limit of 30–50 t h^{-1} estimated by Zhou et al. (2025) for the MTG-FCI geostationary satellite instrument with 3–4 m s^{-1} winds (~10–15 t h^{-1} per m s^{-1} of wind).

Conclusions

We present results from a Very Large Methane Release (VLMR) experiment evaluating methane retrievals from high-detection-limit satellite instruments through coordinated, multi-platform observations of a planned U.S. gas pipeline blowdown event. We used three GOES ABI instruments in five scan modes to continuously monitor emissions with revisit times from 10 minutes to 7 seconds and detected total methane emissions of 370±30 t from two release points over 44–65 min. The blowdown was also observed by six LEO satellite instruments, two aircraft, and a truck-based mobile laboratory. Estimates of total release mass and source rate are generally consistent across measurement platforms and with bottom-up expectations based on operator-reported initial pipeline pressure of 800–950 psi. We find that the satellite detections effectively track the methane pulses downwind, but may underestimate total release mass by ~25% due to late-stage emissions below instrument detection limits. We estimate a GOES ABI plume detection limit of 10–30 t h^{-1} per m s^{-1} of wind for the scene of the experiment. Our results confirm the capability of wide-swath, high-detection-limit satellite instruments to quantify large transient methane releases from low-Earth and geostationary orbit, while highlighting a potential low bias associated with weaker late-stage emissions. Future and retrospective analysis of such events will improve the characterization of retrieval accuracy, precision, and plume detection limits in different observing conditions.

Materials and Methods

Figure 1 depicts the VLMR experimental setup. The blowdown occurred from two release points along the pipeline, hereafter referred to as the eastern and western sources. The satellite, aircraft, and ground-based measurement platforms are described below. Their observational configuration was based on site access constraints, road conditions, and HYSPLIT forecast simulations predicting plume transport and dispersion (Text S1).

GOES ABI GEO satellite data. GOES ABI is a multispectral scanning radiometer with 16 channels in the visible (VIS), near-infrared (NIR), and infrared (IR) that support a wide range of weather, ocean, and environmental monitoring applications. Pixel resolution is 0.5 km (VIS), 1 km (NIR), or 2 km (IR) at equatorial nadir. ABI has three operational scan modes that provide coverage of the full hemispheric disk every 10 minutes, the contiguous US (CONUS) every 5 minutes, and targeted mesoscale sectors (~1000×1000-km2 domain) every 30–60 seconds. GOES-16 operated as GOES-East at 75.2°W from 2016 to 2025, covering the eastern US, Atlantic Ocean, and part of western Africa. It was superseded by GOES-19 in April 2025 and now serves as backup satellite at 104.7°W. GOES-18 currently serves as GOES-West and covers the western US, Pacific Ocean, and Alaska.

At the time of the VLMR experiment, GOES-16 and -18 were in the East and West positions, respectively, and GOES-19 was undergoing commissioning at 90°W. In addition to the operational 5- and 10-min scan modes from GOES-16 and -18, we scheduled 30-s mesoscale scans with GOES-18, and the commissioning of GOES-19 provided an opportunity to test an additional experimental 7-s mesoscale scan mode. We use the Level-1b (L1b) radiances and Level-2 (L2) cloud mask data from a total of five scan modes across all three ABIs to perform methane retrievals for the VLMR pipeline releases with sampling frequencies from 10 min down to 7 s.

GOES ABI can detect large transient methane releases in its shortwave-infrared (SWIR) bands at 1.6 µm and 2.25 µm via multi-band–multi-pass (MBMP) methane retrievals (Watine-Guiu et al., 2023). The retrievals compare images from the methane-sensitive 2.25-µm band with reference images from the 1.6-µm band and previous scans. To retrieve methane column concentrations, we define for each image pixel a band ratio

$$r = \frac{c * R_{2.25}}{R_{1.6}} \text{ (Eq. 2)}$$

where $R_{1.6}$ and $R_{2.25}$ represent the measured radiances in the 1.6-µm and 2.25-µm bands and c is a scaling factor to address differences in scene-wide mean brightness between the two bands. r is converted to methane column enhancement (mol m^{-2}) using a lookup-table derived from radiative transfer calculations. For each resulting retrieval image, we construct a plume-free reference retrieval image from previous (pre-blowdown) scans and subtract it to better isolate methane plumes from surface artifacts (see Text S2 for additional details).

LEO satellite data

TROPOMI. The TROPOspheric Monitoring Instrument (TROPOMI) is a high-spectral-resolution spectrometer on the Sentinel-5P satellite (Veefkind et al., 2012). Its local overpass time is around 13:30 local time (LT) and its methane retrieval product has nadir pixel resolution of 5.5×7 km^2. TROPOMI's fine 0.25-nm spectral resolution enables high-quality methane retrievals with <1% precision (Lorente et al., 2022) and detection of large methane point sources (Schuit et al., 2023). We use the operational TROPOMI L2 total methane column data product (Copernicus Sentinel-5P, 2021) to quantify the total methane mass released during the VLMR experiment (Text S3). TROPOMI's fine retrieval precision makes it an effective baseline for evaluating methane plume mass estimates from less sensitive multispectral retrievals.

VIIRS and SLSTR. De Jong et al. (2025) demonstrated the use of multiple multispectral satellite radiometers for sub-daily monitoring of methane point sources, including VIIRS on the Suomi-NPP, NOAA-20, and NOAA-21 satellites, and the Sea and Land Surface Temperature Radiometer (SLSTR) on the Sentinel-3A and -3B satellites (Pandey et al., 2023). The three VIIRS instruments fly in sun-synchronous afternoon orbits with observations around 13:30 LT, while the SLSTR instruments observe in the morning around 10:00 LT. The methane retrieval algorithm for VIIRS and SLSTR uses the difference of the ratios of reflectance between target and reference images in the 1.6- and 2.25-µm SWIR bands (see Text S4). The nadir spatial resolution of the methane retrieval is 750 m for VIIRS and 500 m for SLSTR. At these resolutions, facility-level methane plumes can be detected, and the sub-daily monitoring frequency combining all instruments makes it possible to capture short-lived emission events such as pipeline blowdowns.

OCI. The Ocean Color Instrument (OCI) is an imaging radiometer on NASA's Plankton, Aerosol, Cloud, ocean Ecosystem (PACE) satellite, launched in February 2024. OCI provides SWIR measurements at 1.6, 2.1, and 2.3 µm with 1.2-km spatial resolution. The 2.1-µm band exhibits weak methane absorption and is spectrally closer than the 1.6-µm band to the methane-sensitive 2.3-µm band, making it a more effective methane-free reference channel for MBMP retrievals. Details about the OCI methane retrieval algorithm are given in Text S5.

Aircraft data

AVIRIS-3. NASA's Airborne Visible/Infrared Imaging Spectrometer-3 (AVIRIS-3) measures contiguous spectra from VIS to SWIR with ~5-nm spectral sampling and supports high-resolution methane point-source detection (Duren et al., 2019; Cusworth et al., 2022). AVIRIS-3 captured a safety test release prior to the full VLMR blowdown at a spatial resolution of 4.2 meters.

Mooney aircraft. NOAA Global Monitoring Laboratory performed ~1 km radius spiral profiles around the two release sites and flew cross-plume transects ~25 km downwind of the western site using a ChampionX Mooney aircraft instrumented with a Picarro 2401-m gas concentration analyzer. Methane mixing ratios were measured every 2.5 seconds and interpolated to 1 Hz, with estimated uncertainties of ±2 ppb. We use these measurements to estimate emission rates Q [kg h-1] for both pipeline release points using a mass-balance approach:

$$Q = \int \left[\frac{M_{CH_4}}{M_{air}} \cdot \rho_{air} \cdot 10^{-9}\right] \cdot [C(t) - C_b] \cdot U_p(t) \cdot dA \quad \text{(Eq.3)}$$

Here C(t) is the measured methane concentration, C_b is the background concentration, $U_p(t)$ is the wind velocity component perpendicular to the plume cross-section, dA is a differential element of the plume cross-sectional area with vertical extent defined by the helix pitch for spirals (Conley et al., 2017) or the boundary layer height for cross-plume transects (Peischl et al., 2015). The factor $\frac{M_{CH_4}}{M_{air}} \cdot \rho_{air} \cdot 10^{-9}$ converts methane mixing ratios from nmol mol^{-1} to mass concentration, where M_{CH4} and M_{air} are the molecular weights of methane and dry air, respectively, and ρ_{air} is the air density (see Text S6).

Ground-based measurements. NOAA Chemical Sciences Laboratory performed ground-based measurements with the Pick-Up Based Mobile Atmospheric Sounder (PUMAS) platform to estimate emission rates from plume transects downwind of the eastern source. PUMAS is a motion-stabilized Doppler lidar (Carroll et al., 2025), augmented for this experiment with an Aeris mid-infrared absorption analyzer measuring methane and ethane at 1 Hz.

We calculate the mass flux for 10-min transects across the eastern plume ~9 km downwind of the source location using the mass-balance approach of Eq. 3, assuming the plume is vertically well-mixed in one vertical layer with cross-sectional area dA. The equation variables are derived from PUMAS measurements of methane mixing ratio, mixed-layer height, and 3D lidar wind fields. The calculated mass flux is assigned to an earlier pipeline release time based on estimated transport time between pipeline and transect (see Text S7).

Data, Materials, and Software Availability

The NOAA GOES Level-1b radiances and Level-2 cloud mask products are publicly available via the AWS Open Data Registry (https://registry.opendata.aws/noaa-goes). TROPOMI Level-2 methane retrievals and Sentinel-3 Level-1 radiances are available from the Copernicus data services (https://www.copernicus.eu). VIIRS and PACE-OCI Level-1 radiances are available from NASA Earthdata (https://earthdata.nasa.gov).

Acknowledgments

We thank Pipeline Research Council International (PRCI) for their assistance coordinating the experiment. The project was supported by NOAA NESDIS (Contract #1332KP24C0023). The views expressed are those of the authors and do not necessarily reflect any position of NOAA or the Department of Commerce. T.A.d J. acknowledges funding from the IMEO Science Studies programme contract DTIE22-EN5036. Part of the work by J.G. was done in the scope of his M.Sc. program at Delft University of Technology. We thank Daniel T. Lindsey for his support in planning the GOES-19 7-second targeted observations.

References

1. Jacob, D. J., Varon, D. J., Cusworth, D. H., Dennison, P. E., Frankenberg, C., Gautam, R., Guanter, L., Kelley, J., McKeever, J., Ott, L. E., Poulter, B., Qu, Z., Thorpe, A. K., Worden, J. R., and Duren, R. M.: Quantifying methane emissions from the global scale down to point sources using satellite observations of atmospheric methane, Atmos. Chem. Phys., 22, 9617–9646, https://doi.org/10.5194/acp-22-9617-2022, 2022.A. V. S. Hill, "HLA associations with malaria in Africa: Some implications for MHC evolution" in Molecular Evolution of the Major Histocompatibility Complex, J. Klein, D. Klein, Eds. (Springer, 1991), pp. 403–420.
2. Fariba Mohammadimanesh, Masoud Mahdianpari, Ali Radman, Daniel Varon, Mohammadali Hemati, Mohammad Marjani, Advancements in satellite-based methane point source monitoring: A systematic review, ISPRS Journal of Photogrammetry and Remote Sensing, Volume 224, 2025, Pages 94-112, ISSN 0924-2716, https://doi.org/10.1016/j.isprsjprs.2025.03.020.
3. Jervis, D., McKeever, J., Durak, B. O. A., Sloan, J. J., Gains, D., Varon, D. J., Ramier, A., Strupler, M., and Tarrant, E.: The GHGSat-D imaging spectrometer, Atmos. Meas. Tech., 14, 2127–2140, https://doi.org/10.5194/amt-14-2127-2021, 2021.
4. Duren, R., Cusworth, D., Ayasse, A., Howell, K., Diamond, A., Scarpelli, T., Kim, J., O'neill, K., Lai-Norling, J., Thorpe, A., Zandbergen, S. R., Shaw, L., Keremedjiev, M., Guido, J., Giuliano, P., Goldstein, M., Nallapu, R., Barentsen, G., Thompson, D. R., Roth,

K., Jensen, D., Eastwood, M., Reuland, F., Adams, T., Brandt, A., Kort, E. A., Mason, J., and Green, R. O.: The Carbon Mapper emissions monitoring system, Atmos. Meas. Tech., 18, 6933–6958, https://doi.org/10.5194/amt-18-6933-2025, 2025.

5. Schuit, B. J., Maasakkers, J. D., Bijl, P., Mahapatra, G., van den Berg, A.-W., Pandey, S., Lorente, A., Borsdorff, T., Houweling, S., Varon, D. J., McKeever, J., Jervis, D., Girard, M., Irakulis-Loitxate, I., Gorroño, J., Guanter, L., Cusworth, D. H., and Aben, I.: Automated detection and monitoring of methane super-emitters using satellite data, Atmos. Chem. Phys., 23, 9071–9098, https://doi.org/10.5194/acp-23-9071-2023, 2023.
6. de Jong, T. A., Maasakkers, J. D., Irakulis-Loitxate, I., Randles, C. A., Tol, P., & Aben, I. (2025). Daily global methane super-emitter detection and source identification with sub-daily tracking. Geophysical Research Letters, 52, e2024GL111824. https://doi.org/10.1029/2024GL111824
7. Watine-Guiu, D.J. Varon, I. Irakulis-Loitxate, N. Balasus, & D.J. Jacob, Geostationary satellite observations of extreme and transient methane emissions from oil and gas infrastructure, Proc. Natl. Acad. Sci. U.S.A. 120 (52) e2310797120, https://doi.org/10.1073/pnas.2310797120 (2023).
8. Zhou, S., Gorroño, J., Roger, J., Irakulis-Loitxate, I., Lindstrot, R., Pei, Z., Si, L., & Guanter, L. (2025). Assessing the potential of the MTG-FCI geostationary mission for the detection of methane plumes (Preprint). EarthArXiv. https://doi.org/10.31223/X5WB32
9. Lauvaux et al. ,Global assessment of oil and gas methane ultra-emitters.Science375,557-561(2022).DOI:10.1126/science.abj4351
10. Ayasse, A. K., Cusworth, D. H., Howell, K., O'Neill, K., Conrad, B. M., Johnson, M. R., Heckler, J., Asner, G. P., & Duren, R. (2024). Probability of detection and multi-sensor persistence of methane emissions from coincident airborne and satellite observations. Environmental Science & Technology, 58(49), 21536–21544. https://doi.org/10.1021/acs.est.4c06702
11. Cusworth, D. H., Jacob, D. J., Varon, D. J., Chan Miller, C., Liu, X., Chance, K., Thorpe, A. K., Duren, R. M., Miller, C. E., Thompson, D. R., Frankenberg, C., Guanter, L., and Randles, C. A.: Potential of next-generation imaging spectrometers to detect and quantify methane point sources from space, Atmos. Meas. Tech., 12, 5655–5668, https://doi.org/10.5194/amt-12-5655-2019, 2019.
12. Gorroño, J., Varon, D. J., Irakulis-Loitxate, I., and Guanter, L.: Understanding the potential of Sentinel-2 for monitoring methane point emissions, Atmos. Meas. Tech., 16, 89–107, https://doi.org/10.5194/amt-16-89-2023, 2023.
13. Sherwin, E.D., Rutherford, J.S., Chen, Y. et al. Single-blind validation of space-based point-source detection and quantification of onshore methane emissions. Sci Rep 13, 3836 (2023). https://doi.org/10.1038/s41598-023-30761-2
14. Worden, J., Green, P., Eldering, A., & Sherwin, E. (2025). Common practices for quantifying methane emissions from plumes detected by remote sensing (NIST Interagency/Internal Report NIST.IR.8575). National Institute of Standards and Technology. https://doi.org/10.6028/NIST.IR.8575
15. Sherwin, E. D., El Abbadi, S. H., Burdeau, P. M., Zhang, Z., Chen, Z., Rutherford, J. S., Chen, Y., and Brandt, A. R.: Single-blind test of nine methane-sensing satellite systems from three continents, Atmos. Meas. Tech., 17, 765–782, https://doi.org/10.5194/amt-17-765-2024, 2024.
16. Tozer, B, Sandwell, D. T., Smith, W. H. F., Olson, C., Beale, J. R., & Wessel, P. (2019). Global bathymetry and topography at 15 arc sec: SRTM15+. Earth and Space Science, 6, 1847–1864. https://doi.org/10.1029/2019EA000658
17. Dowell, D. C., and Coauthors, 2022: The High-Resolution Rapid Refresh (HRRR): An Hourly Updating Convection-Allowing Forecast Model. Part I: Motivation and System Description. Wea. Forecasting, 37, 1371–1395, https://doi.org/10.1175/WAF-D-21-0151.1.
18. C. Frankenberg,A.K. Thorpe,D.R. Thompson,G. Hulley,E.A. Kort,N. Vance,J. Borchardt,T. Krings,K. Gerilowski,C. Sweeney,S. Conley,B.D. Bue,A.D. Aubrey,S. Hook,

& R.O. Green, Airborne methane remote measurements reveal heavy-tail flux distribution in Four Corners region, Proc. Natl. Acad. Sci. U.S.A. 113 (35) 9734-9739, https://doi.org/10.1073/pnas.1605617113 (2016).

19. Jacob, D. J., Turner, A. J., Maasakkers, J. D., Sheng, J., Sun, K., Liu, X., Chance, K., Aben, I., McKeever, J., and Frankenberg, C.: Satellite observations of atmospheric methane and their value for quantifying methane emissions, Atmos. Chem. Phys., 16, 14371–14396, https://doi.org/10.5194/acp-16-14371-2016, 2016.
20. J.P. Veefkind, I. Aben, K. McMullan, H. Förster, J. de Vries, G. Otter, J. Claas, H.J. Eskes, J.F. de Haan, Q. Kleipool, M. van Weele, O. Hasekamp, R. Hoogeveen, J. Landgraf, R. Snel, P. Tol, P. Ingmann, R. Voors, B. Kruizinga, R. Vink, H. Visser, P.F. Levelt, TROPOMI on the ESA Sentinel-5 Precursor: A GMES mission for global observations of the atmospheric composition for climate, air quality and ozone layer applications, Remote Sensing of Environment, Volume 120, 2012, Pages 70-83, ISSN 0034-4257, https://doi.org/10.1016/j.rse.2011.09.027.
21. Lorente, A., Borsdorff, T., Martinez-Velarte, M. C., Butz, A., Hasekamp, O. P., Wu, L., and Landgraf, J.: Evaluation of the methane full-physics retrieval applied to TROPOMI ocean sun glint measurements, Atmos. Meas. Tech., 15, 6585–6603, https://doi.org/10.5194/amt-15-6585-2022, 2022.
22. Sudhanshu Pandey, Maarten van Nistelrooij, Joannes D. Maasakkers, Pratik Sutar, Sander Houweling, Daniel J. Varon, Paul Tol, David Gains, John Worden, Ilse Aben, Daily detection and quantification of methane leaks using Sentinel-3: a tiered satellite observation approach with Sentinel-2 and Sentinel-5p, Remote Sensing of Environment, Volume 296, 2023, 113716, ISSN 0034-4257, https://doi.org/10.1016/j.rse.2023.113716.
23. Duren, R.M., Thorpe, A.K., Foster, K.T. et al. California's methane super-emitters. Nature 575, 180–184 (2019). https://doi.org/10.1038/s41586-019-1720-3
24. Daniel H. Cusworth et al. ,Quantifying methane emissions from United States landfills.Science383,1499-1504(2024).DOI:10.1126/science.adi7735
25. Conley, S., Faloona, I., Mehrotra, S., Suard, M., Lenschow, D. H., Sweeney, C., Herndon, S., Schwietzke, S., Pétron, G., Pifer, J., Kort, E. A., and Schnell, R.: Application of Gauss's theorem to quantify localized surface emissions from airborne measurements of wind and trace gases, Atmos. Meas. Tech., 10, 3345–3358, https://doi.org/10.5194/amt-10-3345-2017, 2017.
26. Peischl, J., Ryerson, T. B., Aikin, K. C., deGouw, J. A., Gilman, J. B., Holloway, J. S., Lerner, B. M., Nadkarni, R., Neuman, J. A., Nowak, J. B., Trainer, M., Warneke, C. and Parrish, D. D. (2015), Quantifying atmospheric methane emissions from the Haynesville, Fayetteville, and northeastern Marcellus shale gas production regions. J. Geophys. Res. Atmos., 120: 2119–2139. doi: 10.1002/2014JD022697.
27. Carroll, B. J., Strobach, E., Baidar, S., Holloway, M. W., McCarty, B., Marchbanks, R., & Brewer, W. A. (2025). Wildfire smoke shading observations: Impacts on boundary layer mixing and thermally driven smoke transport. Journal of Geophysical Research: Atmospheres, 130, e2024JD043303. https://doi.org/10.1029/2024JD043303

Figures and Tables

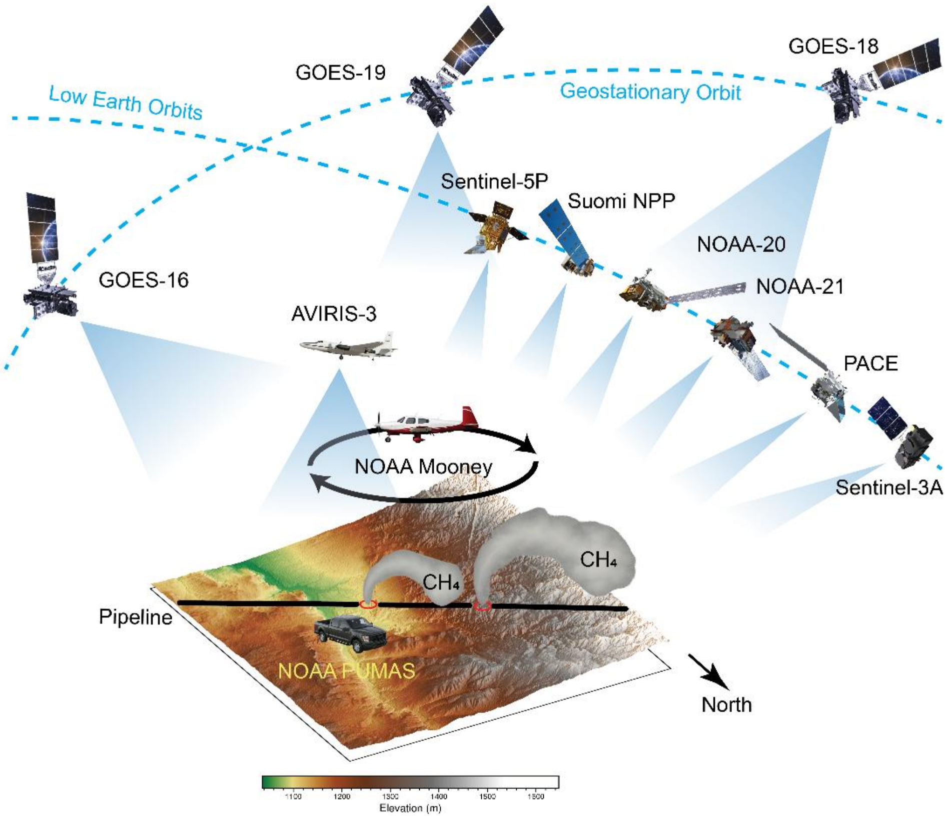

Figure 1. Schematic of the 8 October 2024 VLMR experiment to quantify methane emissions from a planned U.S. gas pipeline blowdown in New Mexico. Measurements were collected from a truck-based mobile laboratory, two aircraft, 3 GEO satellites, and 6 LEO satellites. The basemap shows digital elevation from the Shuttle Radar Topography Mission (SRTM15+ v2.1; Tozer et al., 2019). The red circles indicate the two locations where the pipeline was opened to allow natural gas to escape.

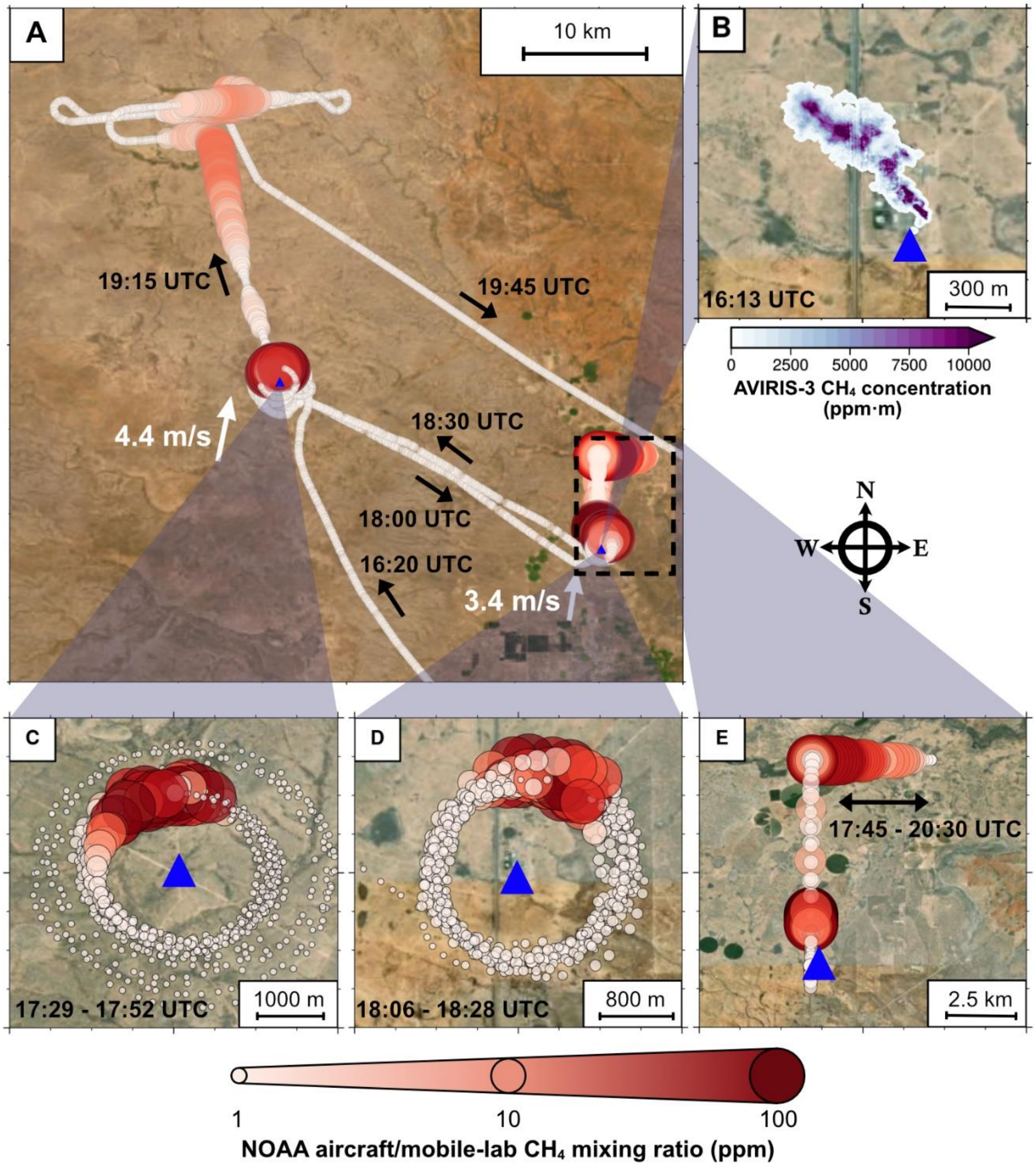

Figure 2. Aircraft and ground-based methane measurements during the VLMR experiment. (A) Methane mixing ratios (ppm) from the NOAA/ChampionX Mooney aircraft and PUMAS mobile laboratory. (B) AVIRIS-3 detection of the pre-blowdown test release. (C–D) Mooney spirals around the western (C) and eastern (D) release sites. (E) PUMAS plume transects within the dashed box in (B) near the eastern site. Blue triangle symbols mark the pipeline blowdown locations. Black arrows indicate direction of the Mooney aircraft and PUMAS mobile lab.

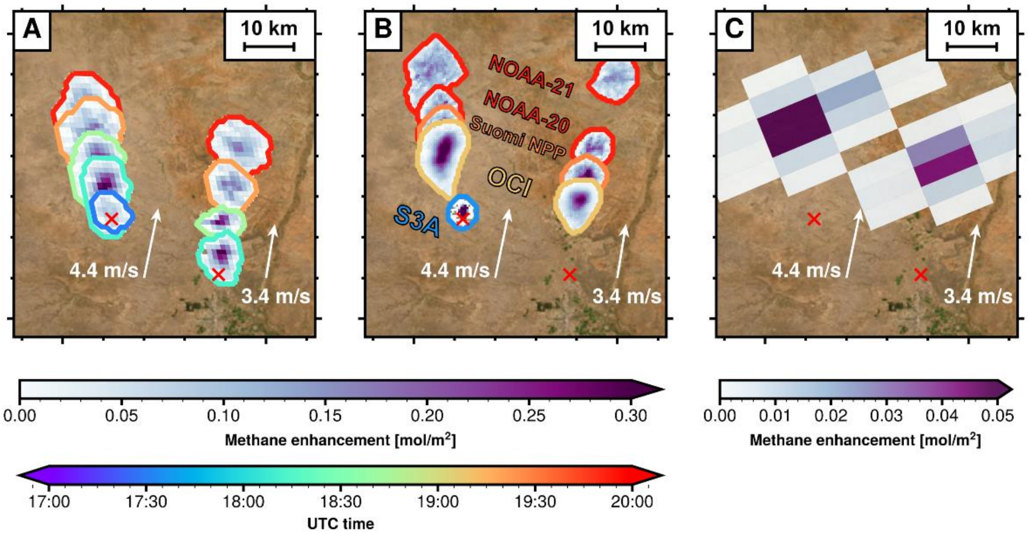

Figure 3. Methane column enhancements retrieved from (A) GOES ABI, (B) VIIRS/SLSTR/OCI, and (C) TROPOMI. The methane plume contour lines in (A-B) are colored by detection time. A NOAA-21 retrieval at nearly the same overpass time as PACE-OCI is not shown in panel (B). TROPOMI observed the scene at approximately 19:30 UTC (13:30 LT). The GOES ABI results in panel (A) are retrieved from GOES-19 measurements and visualized at the 1-km nominal resolution of the 1.6-μm band. Red x symbols mark the two release sites. White vectors are 10-m wind values from NOAA's High-Resolution Rapid Refresh (HRRR; Dowell et al., 2022) data product at the release locations.

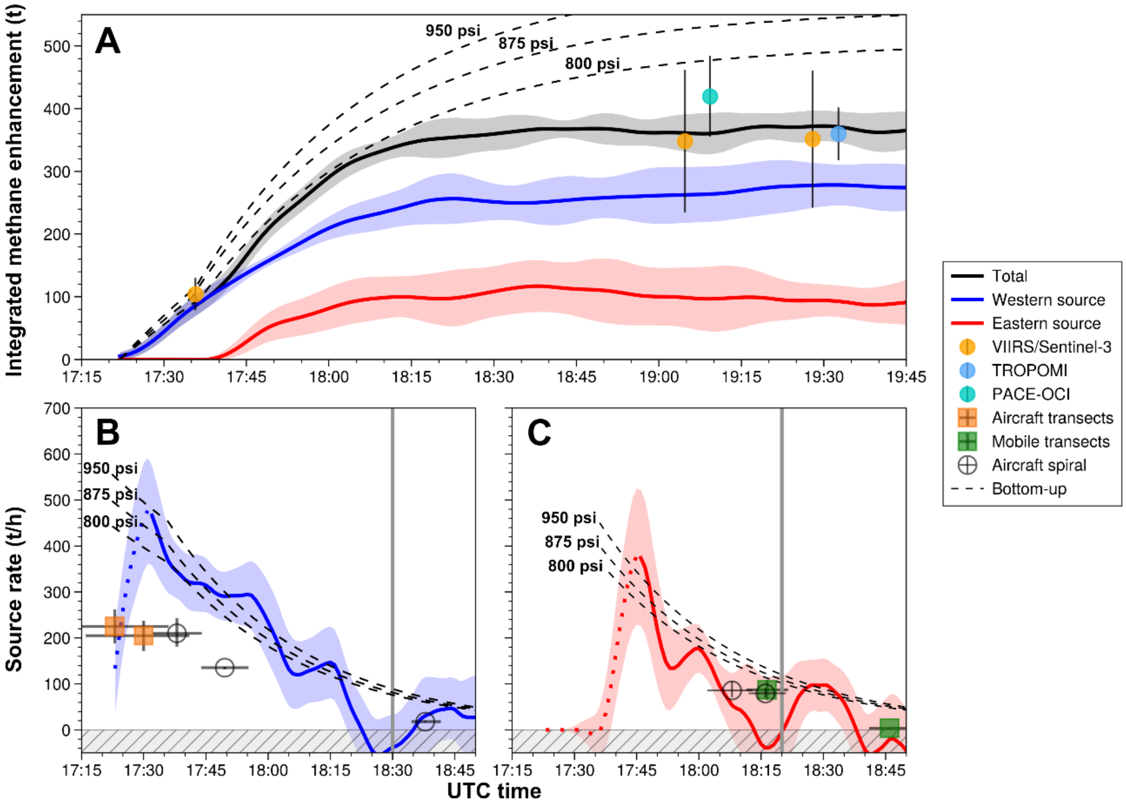

Figure 4. Time series of (A) total methane plume mass (integrated methane enhancement, IME) and (B-C) instantaneous source rate for the western (blue) and eastern (red) sources, defined as the time derivative of IME. Black lines in panel (A) reflect the sum of both plumes. Solid lines are the mean of multiple GOES ABI retrievals interpolated to 1 min and smoothed with a 9-min moving average. Shaded regions denote ±1σ uncertainty ranges derived from the five GOES scan modes. Blue and red dotted line segments in (B, C) mark periods of initial mass accumulation when instantaneous fluxes are not well defined (see text). Black dashed lines reflect bottom-up estimates based on pipeline pressure and volume as described by the operators (see text). Vertical lines in panels (B–C) mark the observed plume detachment times.

Supporting Information for
Coordinated satellite, aircraft, and ground-based observations of a large transient methane release.

Tai-Long He[1], Daniel J. Varon[1,2], Shobha Kondragunta[3], Xinrong Ren[4], Mark D. Cohen[4], Brian J. Carroll[5,6], Nathan Malarich[5,6], Jeffrey Peischl[5,7], Tobias A. de Jong[8], Jelmar Gerritsen[8], Joannes D. Maasakkers[8], Daniel H. Cusworth[9], Riley M. Duren[9], Steven S. Brown[6], Carsten Warneke[6], Colm Sweeney[7], Phillip Stratton[4,10], Alan Brewer[6], Sunil Baidar[5,6], Ezra J. T. Levin[11]

[1]Institute for Data, Systems, and Society, Massachusetts Institute of Technology, [2]Department of Aeronautics and Astronautics, Massachusetts Institute of Technology, [3]NOAA/NESDIS, [4]NOAA Air Resources Laboratory, [5]Cooperative Institute for Research in Environmental Sciences (CIRES), University of Colorado Boulder, [6]NOAA Chemical Sciences Laboratory, [7]NOAA Global Monitoring Laboratory, [8]Space Research Organisation Netherlands (SRON), [9]Carbon Mapper, Inc, [10]Department of Atmospheric and Oceanic Science / Cooperative Institute for Satellite Earth System Studies (CISESS), University of Maryland, [11]Energy Institute, Colorado State University, [12]Department of Systems Engineering, Colorado State University.

*Tai-Long He, Daniel J. Varon
Email: tlhe@mit.edu, dvaron@mit.edu

This PDF file includes:

Supporting text
Figures S1 to S11
Tables S1
Legends for Movie S1
SI References

Other supporting materials for this manuscript include the following:

Movie S1

Supporting Information Text

Introduction.

This Supporting Information includes eight text sections, eleven figures, one table, and one movie.

Text S1 describes the preparation work for the VLMR experiment.
Text S2 describes the lookup-table method used for the GOES ABI retrievals.
Texts S3-S5 provide quantification and retrieval methods for TROPOMI, VIIRS/SLSTR, and PACE-OCI.
Text S6 contains detailed information about the mass-balance calculations of source rates using NOAA Mooney aircraft measurements.
Text S7 provides more details about the NOAA PUMAS mobile lab measurements and mass-balance calculations.
Text S8 discusses the comparison of GOES ABI data streams and the sensitivity test on the moving-average window applied to GOES-18 mesoscale imagery and GOES-19 7-second imagery.

Figure S1 shows an example of forecast plume advection from HYSPLIT simulations used in planning the VLMR experiment.
Figure S2 illustrates the instrumental spectral response functions associated with methane bands on the LEO satellites.
Figure S3 compares the PACE-OCI methane retrievals using the 1.6 μm and 2.13 μm reference bands.
Figure S4 shows the angular wind direction geometry in the aircraft spiral mass-balance calculation.
Figure S5 shows the methodology for estimating the vertical layer thickness for a given aircraft loop in a given vertical profile.
Figure S6 shows the NOAA PUMAS mobile measurements of 3D winds and attenuated aerosol backscatter during the experiment.
Figure S7 shows a schematic of the PUMAS mobile lab driving path and time series of CH4 concentration measurements made from PUMAS.
Figure S8 shows the PUMAS methane and ethane mixing ratio measurements.
Figure S9 shows the time series of PUMAS methane measurements.
Figure S10 shows the performance comparison between the five GOES ABI data streams.
Figure S11 plots the sensitivity test on moving average window size for the GOES-18 mesoscale imagery.

Table S1 summarizes the average error statistics from the sensitivity test on delay time in calibrating aircraft measurements.

Movie S1 shows video footage of the methane plumes derived from GOES ABI.

Text S1: Preparation of the VLMR experiment.

Preparations for the VLMR gas pipeline blowdown experiment involved coordination across multiple NOAA laboratories and collaboration with the gas pipeline operator. Instrument deployment options were evaluated, including aircraft, mobile laboratory, and satellite observations. Site access, road conditions, and expected wind conditions were assessed to determine whether the mobile sampling platform could reliably intercept the plume. To support planning, HYSPLIT forecast simulations were performed in advance to predict plume transport and dispersion (e.g., Figure S1). HYSPLIT simulations were initiated approximately one week prior to the experiment using long-range weather forecast model results and were updated regularly as new meteorological forecast model results became available.

Text S2: GOES ABI retrieval and multi-band-multi-pass (MBMP) approach.

We simplify the GOES ABI retrieval algorithm that was originally based on the band-ratio approach of Varon et al. (2021). Rather than performing a full forward radiative transfer calculation for each pixel, we pre-compute a look-up table (LUT) that maps the observed band-averaged radiance ratio between the 1.6 μm and 2.25 μm ABI channels directly to methane column concentrations, and then correct for viewing geometry with a two-way air-mass factor (AMF). We assume a single US-Standard atmosphere, with background CH_4 = 0.66 mol m^{-2} (~1900 ppb), H_2O = 790 mol m^{-2}, and CO_2 = 143.3 mol m^{-2} (~400 ppm). We ignore vertical structure and also neglect CH_4 absorption in the 1.6 μm band (1–2 orders of magnitude weaker than at 2.25 μm).

The LUT is constructed by computing the top-of-atmosphere radiance in the 2.25 μm methane absorption window for a range of methane slant columns (-1 to +10 mol m^{-2}). For each methane slant column, we use molecular absorption cross sections generated from HITRAN line parameters (via the HAPI Voigt line-shape model) for CH_4, H_2O, and CO_2 at the plume elevation (surface elevation + 0.5 km). We then weight the resulting transmittance by the Kurucz solar spectrum (Clough et al., 2005) across the ABI spectral window at 2.25 μm (2220–2270 nm) to compute the band-mean radiance ratio relative to the background (no CH_4 enhancement) case, and store this forward mapping between slant column and band-mean radiance ratio as the LUT. We then invert this relationship via interpolation, so that observed ABI radiance ratios can be directly mapped to methane slant column enhancement and subsequently converted to vertical column enhancement using the AMF.

For each resulting retrieval image (target), we construct a plume-free reference retrieval image from previous (pre-blowdown) scans and subtract it from the target to isolate methane plumes from surface artifacts. Using the operational 5- and 10-min scan modes, we construct a plume-free reference retrieval image from the average of seven cloud-free scans acquired during the same hour on a previous day when no plume was present, and subtract this reference image from the target retrieval to isolate methane plumes from surface artifacts. For the 30-s and 7-s mesoscale imagery without coverage from previous days, the reference image is instead defined as the mean methane image retrieved from 2 to 1 hours prior to the target scenes. We perform the retrievals and quantify total mass released and emission rate at the native 2-km resolution of the GOES ABI 2.25 μm band.

Text S3: TROPOMI quantification.

An estimate of the Integrated Mass Enhancement (IME) of both plumes at the time of the Sentinel-5P overpass was obtained from the operational TROPOMI CH4 product (Copernicus Sentinel-5P, 2021).

The destriped total column methane data was used. A plume mask was created using a threshold with respect to the median methane concentration of the surrounding pixels (corresponding to a roughly 300km x 300km scene with 710 pixels with successful retrievals), where the threshold (1930 ppb) was chosen to visually match the plume extent.

Methane concentrations were converted to enhancements by subtracting a reference concentration, computed as the median of the scene without the plumes.

Subsequently, the enhancements were converted to per-pixel masses, using the surface pressure from the CH4 product, the area of the footprint of the pixel, and the column averaging kernel of the methane retrieval.

For the column averaging kernel, the plume was assumed to be fully in the lowest layer of the TROPOMI retrieval (corresponding to the layer up to around 750m above the surface). The IME was then computed by summing this value for all pixels in the plume.

Uncertainties were computed by propagating the standard deviation of the concentration of the background pixels and the uncertainty of the CH4 retrievals within the plumes as independent contributions.

Text S4: VIIRS/SLSTR retrieval and quantification

For VIIRS and SLSTR, methane enhancements were retrieved with a Multi-Band Multi-Pass method, slightly adapted from the one described by de Jong et al., 2025. Two adaptations were made, both improving internal consistency.

First, we used the following formula for the MBMP signal:

$$\Delta R_{MBMP} = \frac{c_{2.2} R_{2.2}}{R_{2.2}{}'} - \frac{c_{1.6} R_{1.6}}{R_{1.6}{}'}$$

where the constants c_i are the ratios of the median values of the band radiances on the reference day R*i*' and on the measurement day R*i* for the band with wavelength *i* µm. We then performed radiative transfer simulation to estimate methane concentration fields using ΔR_{MBMP}.

Second, an additional median subtraction was performed. The MBMP method yields methane enhancements with respect to an arbitrary reference concentration. To more accurately compute the enhancement in the plume, after finding the plume masks, the median of the pixels in the scene outside the plume masks was subtracted before computing the IME.

Otherwise, the same methods as in de Jong et al. (2025) were used, including destriping and resampling to a 500m-resolution grid of roughly 100 km x 100 km.

The plume mask was also found using the same methods, by normalizing the enhancements with respect to the uncertainty and selecting areas with a deviation of more than 1.5 standard deviation and selecting only the two largest such areas per overpass. The uncertainty was similarly computed by summing the per-pixel uncertainties.

Text S5: PACE-OCI retrieval

Methane enhancement retrievals were also performed using the Ocean Color Instrument (OCI) aboard the Plankton, Aerosol, Cloud, ocean Ecosystem (PACE) satellite, which launched on the 8th of February 2024. OCI has a nominal resolution of 1.2 km and has three SWIR bands relevant for methane retrievals: bands F, H and I, centered at 1.62, 2.13 and 2.26 µm respectively, as shown in Figure S2.

The same retrieval method described in Text S4 was used, but using bands H and I. Data was resampled to the same 500m-resolution grid used for the VIIRS retrievals.

As the H band is much closer to the I band compared to the usual 1.6 µm reference band used for other instruments, this combination is less sensitive to artifacts such as caused by differences in relative albedo of the surface, as illustrated in Figure S3. This smaller difference results in a cleaner retrieval. The OCI data was subsequently processed using the approach used for the VIIRS/SLSTR data as described in Text S5.

Text S6: NOAA/ChampionX Mooney Aircraft Measurements and Mass Balance Calculation

The NOAA/ChampionX Mooney aircraft flew ~1-km-radius loops around the western and eastern sources at different altitudes to create vertical profiles of downwind concentrations from each source. Six profiles were conducted around the West source, and two around the East source. CH_4 emissions rates were calculated for each profile by summing the second-by-second mass flow rates in each individual loop within a given profile.

Four different methods were used in the calculations to estimate the uncertainty in the mass-balance methodology for each loop: (1) the base method, using the loop average wind speed and wind direction as calculated from the aircraft GPS readings; (2) wind speed as in (1) but wind direction calculated as the concentration-weighted aircraft orientation relative to the source, i.e., the wind direction that would cause the plume to end up where it was measured; (3) wind speed and wind direction from the NOAA National Weather Service (NWS) High Resolution Rapid Refresh forecast model (HRRR); and (4) wind speed and wind direction from the NOAA NWS forecast North American Model (NAM).

The mass-balance methodology considers a cylindrical control surface around the emissions site. To estimate the mass flow rate through this cylindrical surface for a given loop, we sum the mass flow rate through the surface for each second during the loop, factoring in the estimated vertical thickness h of the layer that the loop is assumed to represent.

In the following equation, for a given loop, the summation goes from the start time of the loop (0) to the end time of the loop (T).

$$\sum_0^T [C(t) - C_b(t)] \cdot \Delta w(t) \cdot \Delta h \cdot U_p(t) \cdot \beta(t) \quad \text{(Eq. S1)}$$

where

$C(t)$ (μmol CH_4 / mol air) = the second-by-second concentration of CH_4 measured during the loop by the Mooney aircraft;

$C_b(t)$ (μmol CH_4 / mol air) = the estimated background concentration of CH_4 during the loop;

$\Delta w(t)$ (m) = the second-by-second distance that the aircraft travelled during the loop;

$\Delta h(m)$ = the estimated vertical thickness of the vertical layer associated with the loop;
$U_p(t)$ (m s^{-1}) = the second-by-second component of the horizontal wind velocity perpendicular to the direction of the aircraft at the location of the aircraft concentration measurement during that second (see Figure S4 below);
$\beta(t)$ [g m^{-3} / (μmol CH_4 / mol air)] = the second-by-second factor to convert from the volume/volume concentration measurements to mass/volume concentration values.

Since the control surface is a cylinder, we have used the orientation of the sampling site relative to the emissions source rather than the aircraft's heading relative to the ground, although the difference between the two is generally very small. It should be noted that the distance from the source varied during each loop, i.e., the cylinder's cross-section was not a circle. For each one-second measurement, the horizontal distance traveled was calculated as the radial distance for that measurement multiplied by the change in angle relative to the source location during that measurement.

Further, it should be noted that the elevation of each loop was not constant. For each loop, a concentration-weighted average elevation was used. This methodology ensures that the loop elevation used in the overall mass balance calculation reflects the measurements with strongly elevated CH_4 concentrations.

The mass flow rate for a given loop is then related to the time-resolved emissions rate from the source by subtracting an estimate of the travel-time from the source to the loop.

In the sections below, more details regarding the methodology are presented.

Text S6.1: Loop by Loop Analysis

Distinct loops were defined around the eastern and western source locations, in which the aircraft distance from the source was less than 2 km throughout the loop.

The start of each East loop was assumed to be at an aircraft orientation relative to the source of ~58 degrees (the aircraft was approximately West-Southwest of the site). At that location, the wind direction would have had to be ~58 degrees for the wind to blow directly from the source location to the aircraft location.

The start of each West loop was assumed to occur at a comparably defined orientation of ~325 degrees when the aircraft was Southeast of the West emissions site. This value ensured that the enhanced methane concentrations measured, at roughly 180 degrees, were well separated from the start and end of each loop. Also, the first loop around the West emissions site started at about 325 degrees.

Text S6.2: Vertical Layer Thickness Associated with Each Loop in a Given Profile

The vertical layer thickness represented by a given loop in a given profile is assumed to be the difference in elevation from the midpoint between the loop and the next lowest-elevation loop and the midpoint between the loop and the next highest elevation loop in that profile. For the lowest elevation loop in a profile, the layer is assumed to extend to the surface. For the highest elevation loop, the layer is assumed to extend the same vertical distance above the loop as the difference in the loop elevation between the loop and the midpoint between the loop and the next lowest-elevation loop. This aspect of the methodology is shown schematically in Figure S5.

Text S6.3: Time Lag for Aircraft Measurements

The aircraft GPS-associated measurements (lat, long, u, v, altitude, etc.) were delayed approximately 4-7 seconds due to data-processing and transfer constraints. The physical and chemical measurements (P, T, RH, CH_4-ppbv, etc.) were delayed approximately 11 seconds primarily due to the inlet length. In the merged dataset from the aircraft flights, the physical and chemical measurements are automatically adjusted for the 11-second inlet-related delay. To match the GPS data to the physical-chemical measurement data, a specified number of seconds must be subtracted from each GPS timestamp's "UTC-Start" (seconds).

Numerical sensitivity experiments were conducted for GPS delays of 4, 5, 6, and 7 seconds to calibrate aircraft wind direction measurements. A statistical summary for the entire series of numerical experiments is shown in Table S1. Based on these results, a GPS time lag of ~6 seconds was used as the "base" value in this analysis. However, the emissions rates estimated with time lags of 4-7 seconds are relatively consistent, and the sensitivity to this assumption is not large.

Method 1 (base method). Wind speed and direction associated with each one-second CH_4-ppbv measurement are assumed to be the loop average wind speed and wind direction, based on the second-by-second u and v measurements reported by Aspen Avionics.

Method 2. Wind speed associated with each one-second CH_4-ppbv measurement is assumed to be the loop average wind speed, based on the second-by-second u and v measurements reported by Aspen Avionics.

Wind direction associated with each one-second CH_4-ppbv measurement is assumed to be the concentration-weighted average direction associated with each measurement, i.e., the wind direction from the source that would cause the plume to end up where it did, relative to the source.

Method 3. Wind speed and wind direction associated with each one-second CH_4-ppbv measurement are based on archived quasi-analysis HRRR wind speed and wind direction, interpolated in space to the relevant source location (East or West) and interpolated in time between the 1-hour snapshot outputs from the HRRR model. The HRRR model data is converted to HYSPLIT format and archived at the native 3 km horizontal resolution. The HRRR model is run every hour, and the 2nd hour of each forecast cycle is saved for the HYSPLIT HRRR archive at hybrid sigma/pressure vertical levels (https://www.ready.noaa.gov/data/archives/hrrr/README.TXT).

Method 4. Wind speed and wind direction associated with each one-second CH_4-ppbv measurement are based on archived quasi-analysis NAMS wind speed and wind direction, interpolated in space to the relevant source location (East or West) and interpolated in time between the 1-hour snapshot outputs from the NAMS model. The NAMS model data are converted to HYSPLIT format and archived at a 12 km horizontal resolution, which is lower than the native 3 km resolution. The NAM model is run every 6 hours, and the first 6 hours of each forecast cycle are saved for the HYSPLIT NAMS archive, on hybrid sigma/pressure vertical levels (https://www.ready.noaa.gov/data/archives/nams/README.TXT).

Text S6.4: CH_4 Background

Each loop took on the order of ~80 seconds to complete, and during each loop, CH_4 enhancements were measured at 15-20 seconds during the loops. The CH_4 background for each aircraft loop was estimated as the 40th percentile of concentration values in that loop. Using other non-enhanced percentile values to characterize the non-enhanced "background concentrations" made only a trivial difference in the mass- balance emissions estimates and is not considered an important uncertainty in the mass- balance calculations.

Text S6.5: Measurement Time vs. Emissions Time

The emission time for a given source differs from the aircraft measurement time because it takes time for the plume to travel from the source to the concentration measurement location.

To estimate the uncertainty range in the travel time, we have estimated the minimum emissions time for a given profile by subtracting the maximum loop travel times (distance from source divided by the minimum loop wind speed (from methods 1, 2, 3, and 4)) from the time of the first loop in a given profile.

The maximum emissions time for a given profile was estimated by subtracting the minimum loop travel times (distance from source divided by the maximum loop wind speed, from methods 1, 2, 3, and 4) from the time of the last loop in a given profile. The range in possible emissions times estimated in this way is used to estimate the uncertainty in the emissions time for any given profile.

Text S6.7 Additional Emissions Estimates Based on a Mass-Balance Analysis of Downwind Aircraft Transects

After flying multiple cylindrical spirals around the two release point locations, the aircraft flew 25 km downwind of the western point source and performed two crosswind transects at 375 and 510 m agl. The planetary boundary layer depth was determined from a vertical spiral in the middle of the plume after these transects. A methane mass balance was calculated for each downwind transect following the methods of Peischl et al. (2016):

$$flux = vcos(\alpha) \int_{z_0}^{z_1} \int_{-y}^{y} (CH_4 - CH_{4,bg})\ dy\ dz$$

where z_0 is the ground level, z_1 is the adjusted mixing height, $CH_{4,bg}$ is the background CH_4 value, and vcos(α) is the wind speed velocity perpendicular to the flight path.

The well-mixed PBL depth was determined to be 1203 m agl from the vertical profile data. The entrainment height was determined to be 1632 m agl. From these, we calculate an adjusted mixing height, z_1, of 1315 m agl following Peischl et al. (2015) Equation 2, reproduced here:

$$z_1 = z_{PBL} \times \{1 + [\frac{[z_e - z_{PBL}](CH_4 - CH_{4,bg})}{4}]/[(z_{PBL} - z_0)(CH_4 - CH_{4,bg})]\}$$

where z_1 is the adjusted mixing height, z_{PBL} is the location of the top of the PBL, z_e is the entrainment height, where the enhancement in the PBL reaches the free tropospheric value, and z_0 is the ground level.

The NOAA/ChampionX Mooney aircraft reports a wind speed uncertainty of ±0.2 m/s (Conley et al., 2014). For the western plume, we take the average wind speed of 3.7 m/s, which includes wind measurements from the time spent on the four near-field spirals, the time traveling to the downwind transects, and the time in the downwind transects, which encompasses approximately 50 minutes of wind measurements. We double the wind speed uncertainty to account for the plume transit time when the Mooney aircraft was flying elsewhere. From the wind speed and distance downwind, we estimate the first plume transect to be 6976 +787/-849 seconds from the time of emission, and the second plume transect to be 6861 +672/-834 seconds from the time of emission.

The uncertainty of the CH4 background is estimated to be ±5 ppb, and the accuracy is estimated at ±2 ppb relative to the WMO X2004A scale. These uncertainties are considered negligible relative to the enhancement of greater than 6 ppm in the plumes. All CH4 data are reported as dry air molar ratios.

Text S7: NOAA PUMAS Mobile Lab

The NOAA Chemical Sciences Laboratory (CSL) Pick-Up Based Mobile Atmospheric Sounder (PUMAS) is a fully mobile truck platform that primarily hosts a Doppler lidar, and was supplemented with an in situ methane and ethane instrument for this project. The Doppler lidar provides profiles of horizontal wind vectors and the vertical wind (w) above the truck while stationary and underway, using separate lidar channels dedicated to scanning for horizontal winds and staring for vertical. This unique capability provides 3D winds and aerosol backscatter at 0.045 Hz above the truck with 60-m vertical resolution at all times. The lidar pointing is stabilized against pitch and roll of the truck in real-time by housing the lidar optics in a motion stabilization platform in the truck bed. The orientation and velocity of the truck and lidar optics are tracked to remove the platform motion projection into the measured line-of-sight lidar velocity. More information is available in Carroll et al., 2025.

The lidar wavelength is 1.54 μm, and thus the signal-to-noise ratio is particularly sensitive to aerosols. The combined dynamics and aerosol information enables a robust boundary layer height retrieval based on mixing (e.g., *w* variance), wind shear, and aerosol gradient (Tucker et al., 2009). Figure S6 shows the wind and aerosol measurements from this experiment. The range resolution of both lidar channels was 62 m and the temporal resolution was 15 seconds for each profile of horizontal winds (i.e., one conical scan) and 1 second for the vertical wind channel. The wind speed shows a very consistent and well-defined low level jet in the morning before sunrise, which decays as the daytime well-mixed boundary layer starts to grow. Boundary layer winds strengthened gradually from morning to midday. The boundary layer height grew substantially over the study period (17:36 - 19:00 UTC), making this measurement essential for accurate retrievals of methane emissions.

An Aeris instrument was deployed on PUMAS to measure methane and ethane at 1 Hz. The analyzer is a high-precision trace gas instrument based on mid-infrared (mid-IR) laser absorption spectroscopy for continuous, real-time measurements of methane and ethane (C_2H_6). By targeting fundamental vibrational absorption features in the mid-IR spectral region, the analyzer achieves high selectivity and sensitivity with low cross-interference from other atmospheric gases. The instrument offers sub-ppb detection limits, rapid time response (1 s), and stable operation suitable for both laboratory and field deployments. Its applications include urban air quality monitoring, natural gas leak detection, and characterization of methane sources, with ethane serving as a tracer to help distinguish fossil fuel emissions from biogenic methane. The analyzer was calibrated before and after the pipeline blowdown experiment. An online zeroing system was incorporated to zero the analyzer using ultra-zero air to track instrument drift during operation.

Text S7.1: Summary of the Mass Balance Methodology Used to Estimate Emissions Based on the Mobile Lab Measurements

Similar to Eq.S1, we consider a plane (curtain) downwind of the emissions site and calculate the mass flow rate through this plane. We do this by summing the mass flow rate through the plane for each second during a given transect. In the following equation, for a given transect, each term is a function of time, and the summation goes from the start time of the transect (0) to the end time of the transect (T).

$$\sum_0^T [C(t) - C_b(t)] \cdot \Delta w(t) \cdot \Delta h \cdot U_p(t) \cdot \beta(t) \text{ (Eq. S1)}$$

where

$C(t)$ (μmol CH_4 / mol air) = the second-by-second concentration of CH4 measured during the transect;

$C_b(t)$ (μmol CH_4 / mol air) = the second-by-second background concentration of CH4 during the transect;

$\Delta w(t)$ (m) = the second-by-second distance that the mobile lab travelled during the transect;

Δh(m) = the second-by-second height of the plume at the location of the concentration measurement location during that second;

$U_p(t)$ (m s^{-1}) = the second-by-second component of the horizontal wind velocity perpendicular to the direction of the mobile lab at the location of the concentration measurement during that second;

$\beta(t)$ [g m^{-3} / (μmol CH_4 / mol air)] = the second-by-second factor to convert from the volume/volume-based concentration measurements to mass/volume concentration values.

The mass flow rate for a given transect is then related to the emissions rate from the source by subtracting an estimate of the travel-time from the source to the transect, i.e., to account for the fact that the measurements occurred after the plume had traveled for some time downwind of the source.

We carried out an extensive series of numerical experiments and sensitivity analyses with respect to how the terms in Equation S2 were calculated, and on the basis of this analysis, we estimate the overall uncertainty in the mass-balance flux estimates for each mobile transect to be ± 25%.

Text S7.2: Transect by Transect Analysis.

The mobile lab primarily drove along a north-south road (the blue road in Figure S7, upper left schematic) and an east-west road (the red road in Figure S7, upper left schematic). The transects occurred along the east-west road about 9 km downwind of the source. The mobile lab driving path can be divided into 7 sections, as shown in Figure S7 (lower panel).

The methane fluxes were calculated using Eq. S2, with $\Delta h(t)$ set as the lidar-determined mixing height. We fit a seventh-order polynomial to $\Delta h(t)$ in Figure S6 to time-interpolate a time-varying h across each transect. To get the boundary-layer averaged wind U_p in Eq. S2, we vertically-average the wind profiles between ground and mixing height $\Delta h(t)$, time-average nearby profiles (using a low-pass filter) to remove turbulent noise, then curve-fit to match their time-evolution with the 1 Hz methane measurements.

The PUMAS drive route and the in situ concentrations are shown in Figure S8, with the methane time series also shown in Figure S9. The PUMAS truck was near the eastern release site at the time of release, then, given the approximately southerly wind direction, PUMAS drove north with the goal of executing cross-plume transects far enough downwind that the methane would be well-mixed within the boundary layer. The first large plume intercept while driving north was incidental and did not transect the entire plume width, so it is not suitable for a representative emissions estimate. The later east-west legs are useful for emissions estimates, as the data shows that all or at least more than half of the plume was transected each time. The distance between the eastern release site and the east-west transects is ~8.5 km, which corresponds to ~28–35 minutes of transport time, given average winds of 4-5 m/s measured in the PBL. This is enough time for two eddy turnovers, and the observed plume widths are ~3x the mixing height. Both are good indicators of the vertically well-mixed assumption. These transect estimates are also shown in Figure 2 in the main text.

Text S7.3: Estimation of Travel Time of the Plume

In order to relate the mass flux estimated from the mobile-lab transect to the emissions time of the source emissions, the travel time of the plume from the source to the transect must be subtracted from the transect time.

To estimate the travel time, we integrated the PUMAS wind backwards in time from the measurement time average, and determined when the integral reached the distance between the concentration-weighted transect location and the release point. This methodology may lead to an underestimate of the travel time because the plume likely did not follow a perfectly straight line from the source to the transect. This analysis gives an estimated travel time of ~30 minutes for Transect 01, and ~26.5 minutes for Transect 02.

Text S8: Comparison between GOES ABI data streams and sensitivity test on moving averaging

As shown in Figure S10, we compare the performance of different GOES ABI data streams by calculating the signal-to-noise ratio (SNR) and the root mean square error (RMSE) for each scan. The SNR is defined as follows:

$$SNR = 10 \times \log_{10} \frac{P_{signal}}{P_{noise}}$$

where P_{signal} is the average power of the isolated plume signal with non-plume pixels replaced by zeros and P_{noise} is the average power of background pixels (masking out plumes, water body, and clouds). Here we define the powers of imagery as

$$P_{signal} = \sum_{i,\ in\ plume} x_i$$

$$P_{noise} = \sum_{i,\ in\ background} x_i$$

A higher SNR indicates a stronger ability to isolate plume signals from the background, while a lower RMSE reflects greater precision in methane retrieval. The GOES-18 mesoscale imagery shows the best performance in both isolating plume signals and retrieving methane with high precision. The GOES-19 7-second imagery performs comparably to the GOES-18 and GOES-16 full-disk imagery, whereas the GOES-16 CONUS scans exhibit lower SNR and higher RMSE.

The smoothed GOES-18 mesoscale retrievals outperform all operational data streams, increasing the SNR from -13 and -10 to values above -18 and reducing the RMSE by 50%, from 0.08 mol m^{-2} to below 0.04 mol m^{-2}. We also performed a sensitivity test on the choice of window size for smoothing the GOES-18 mesoscale retrievals. As shown in Figure S11, we find that both SNR and RMSE improve as the GOES-18 mesoscale imagery is averaged from 1-min to 2-min, and further to 5-min and 10-min windows. The best performance is achieved with 5-min and 10-min windows, which yield nearly identical results. For consistency, we adopt the 5-min window in the main text.

Figures

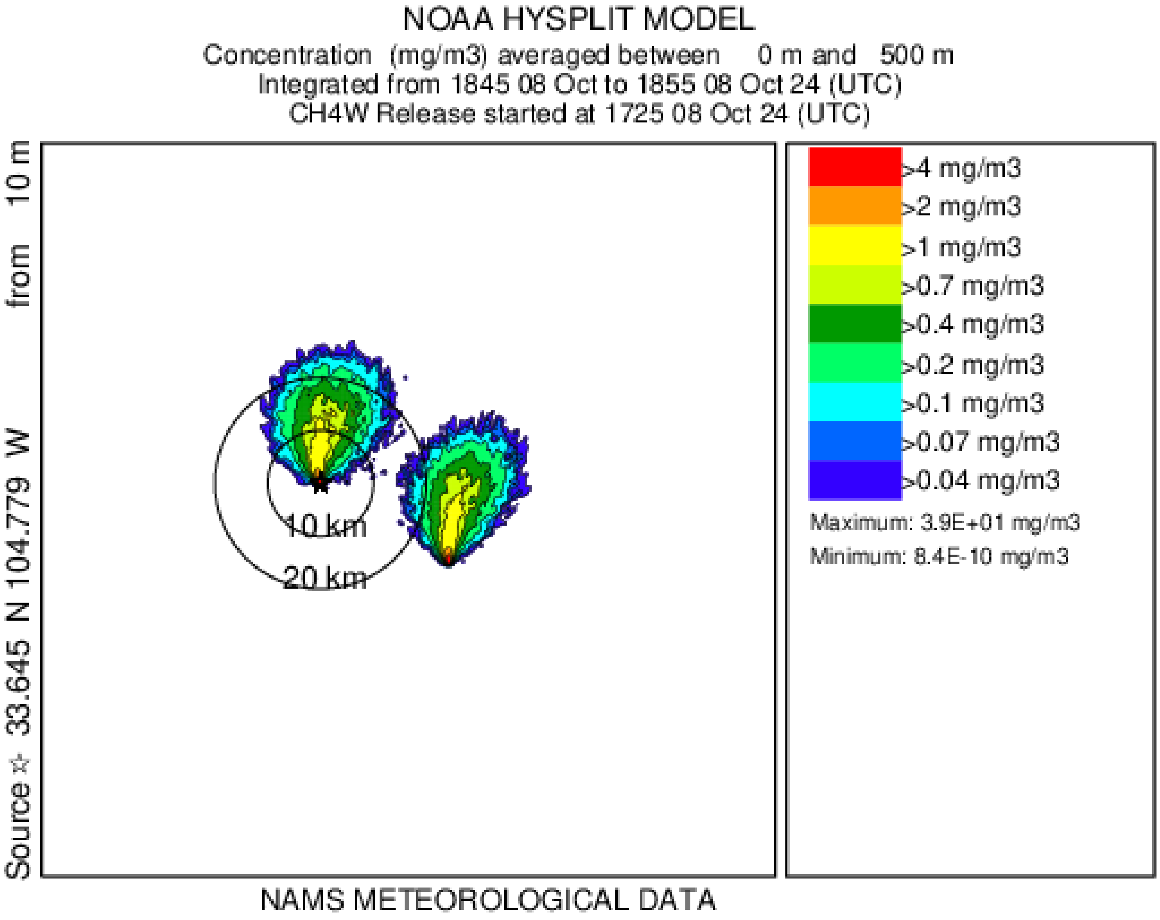

Fig. S1. Example of HYSPLIT-simulated forecast concentrations, based on forecast meteorology, used for planning before the event started. This forecast graphic covers a 10-minute period from 1845-1855 UTC, which would occur during the 2nd hour of the actual event. The actual forecast graphic for field use included much more information (lat/longs, roads, etc.). The simplified version shown here does not include geolocation information, due to restrictions on the release of proprietary business information.

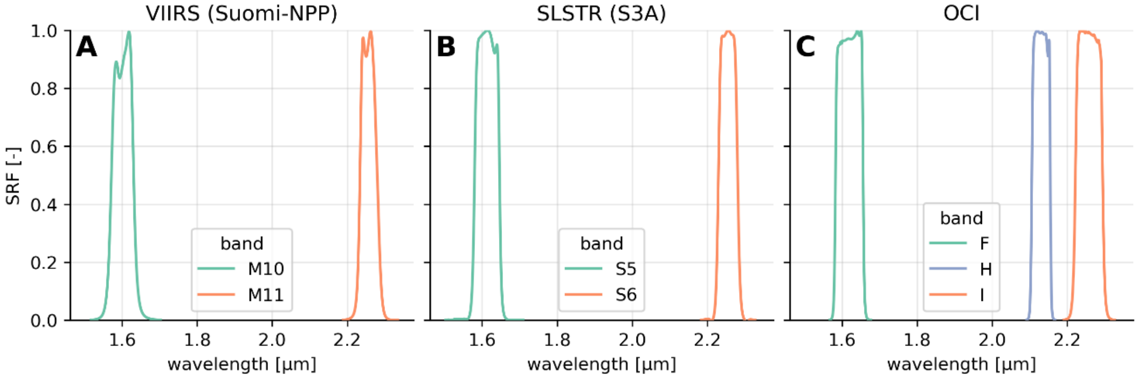

Fig. S2. Instrument Spectral Response Functions (SRFs) of bands relevant to methane retrieval for (A) VIIRS on Suomi-NPP, (B) SLSTR on S3A and (C) OCI on PACE. SRFs for OCI were sourced from Meister et al. (2024).

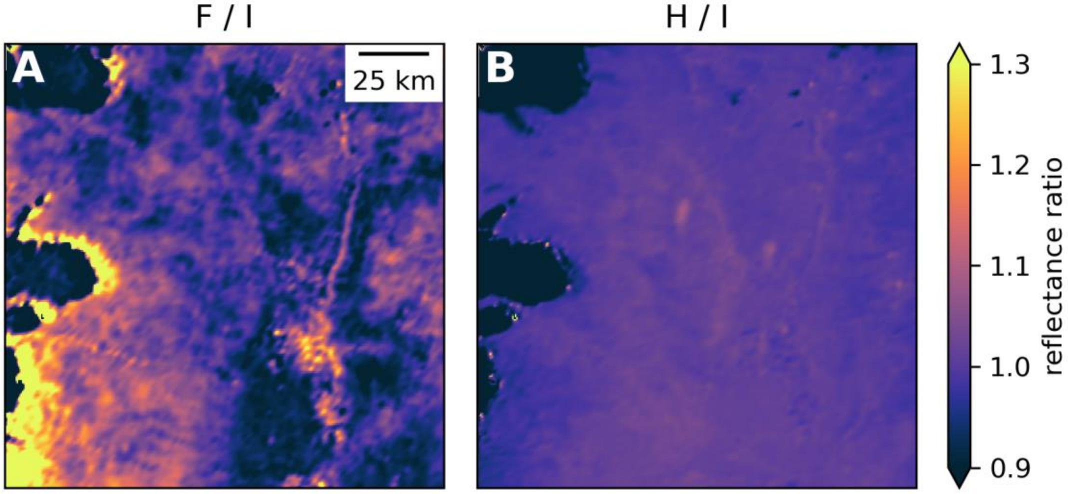

Fig. S3. Ratios of reflectance measured in different SWIR bands of PACE-OCI for the overpass of the VLMR event. Comparing the usual 1.6 µm reference band (band F on PACE-OCI) and the 2.13 µm band (band H on PACE-OCI) to the 2.26 µm band (band I on PACE-OCI), which has the strongest methane absorption. Shown are (A) band F over band I and (B) band H over band I.

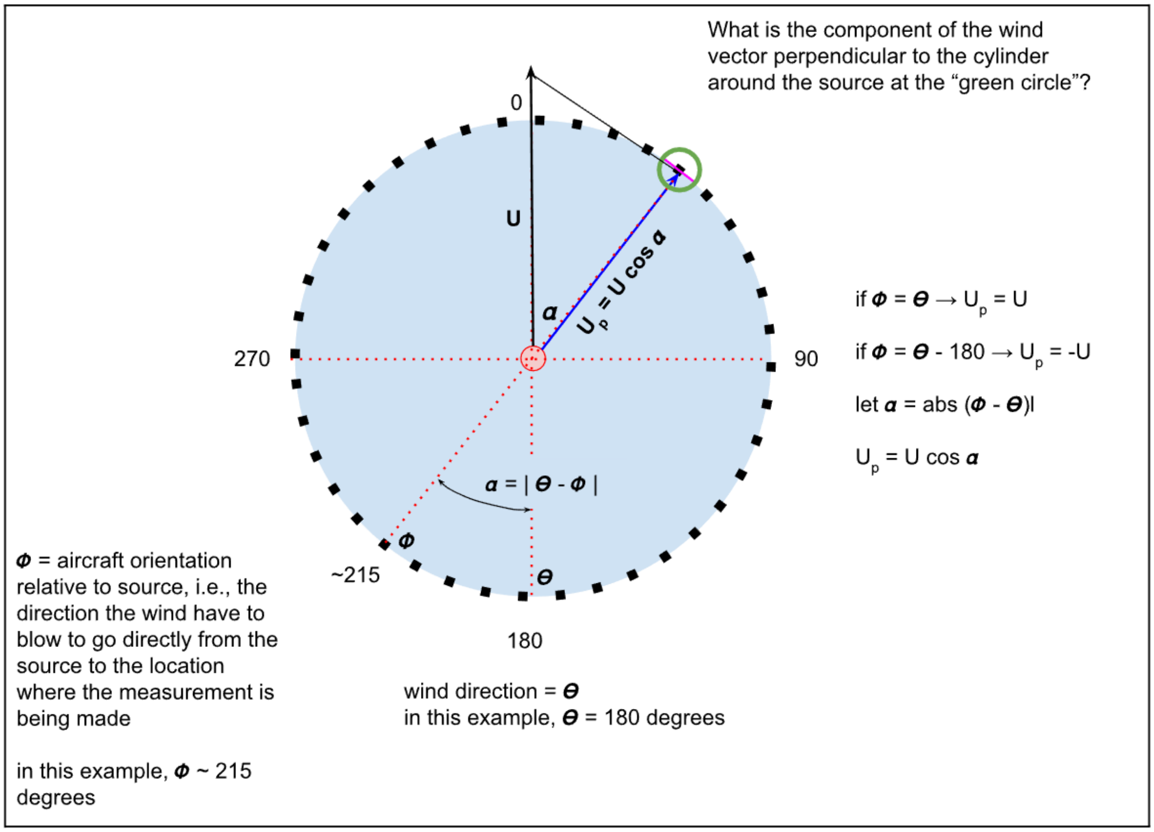

What is the component of the wind vector perpendicular to the cylinder around the source at the “green circle”?

if $\Phi = \Theta \rightarrow U_p = U$

if $\Phi = \Theta - 180 \rightarrow U_p = -U$

let α = abs ($\Phi - \Theta$)l

$U_p = U \cos \alpha$

Φ = aircraft orientation relative to source, i.e., the direction the wind have to blow to go directly from the source to the location where the measurement is being made

in this example, Φ ~ 215 degrees

wind direction = Θ
in this example, Θ = 180 degrees

Fig. S4. Angular wind direction factor in mass balance calculation.

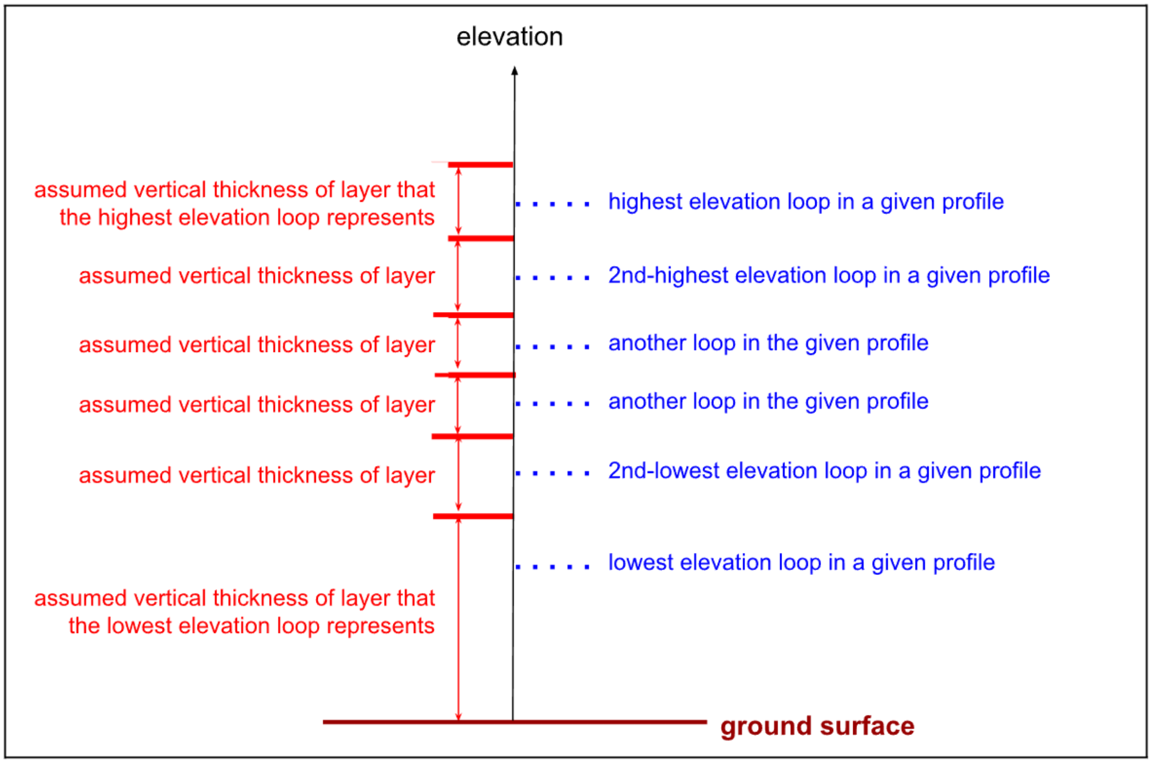

Fig. S5. Vertical layer thickness estimation for a given loop in a given profile.

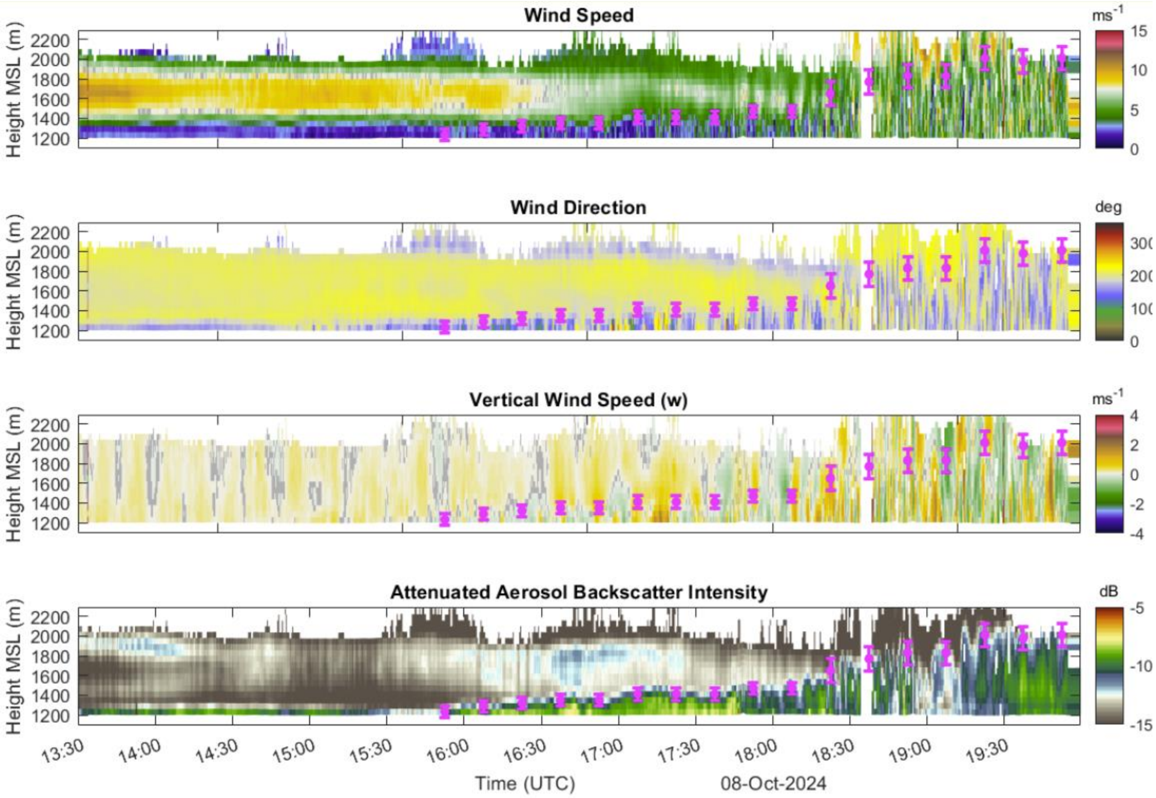

Fig. S6. PUMAS lidar profile time series of (a) wind speed, (b) wind direction, © vertical wind, and (d) attenuated backscatter during the experiment. The pink points are boundary layer heights with uncertainty bars.

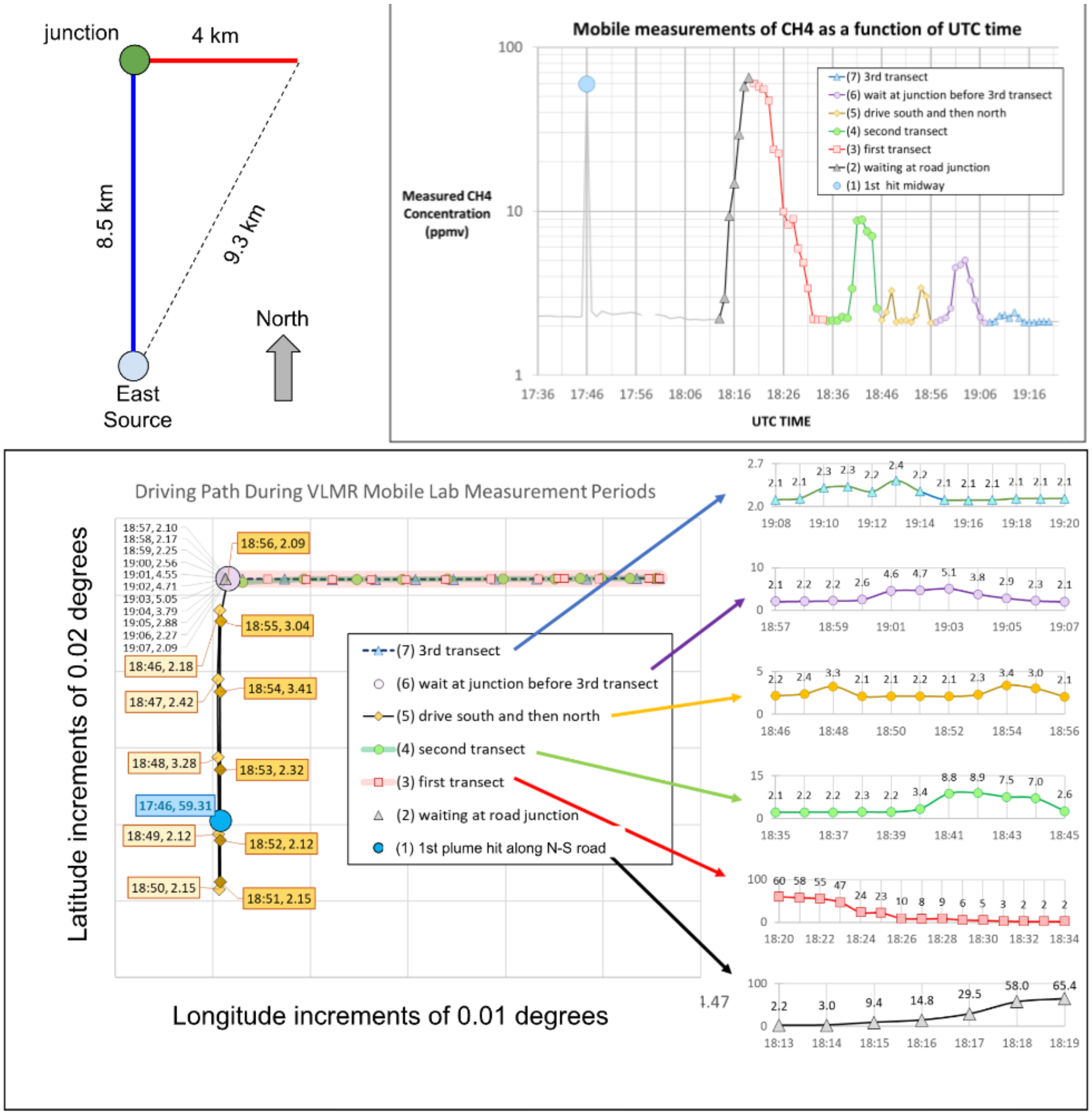

Fig. S7. (Top) Schematic of the PUMAS mobile lab driving path and time series of CH4 concentration measurements made from the mobile lab. (Bottom) Seven segments of the mobile lab driving path and associated CH4 measurements.

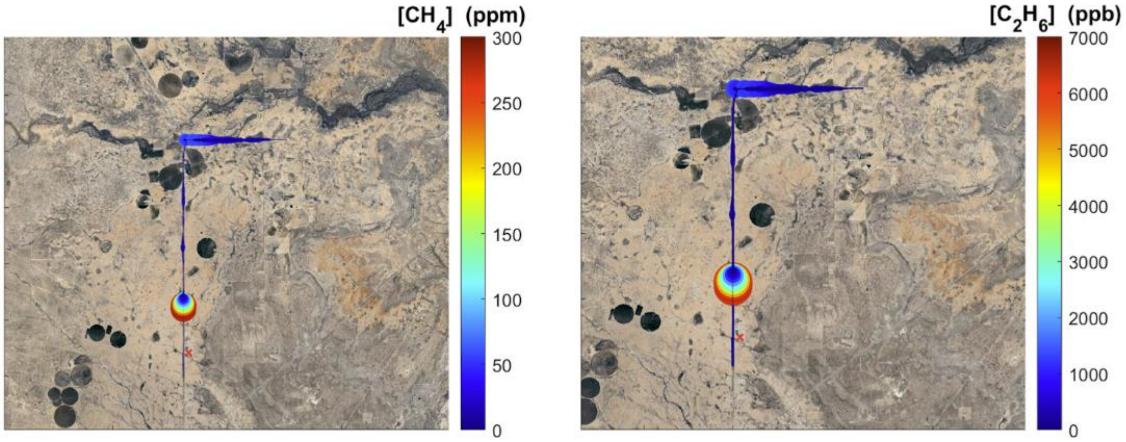

Fig. S8. Methane and ethane mixing ratios measured along the driving track during the pipeline blowdown experiment on Oct 8, 2024. The red cross marks the location of the eastern release facility.

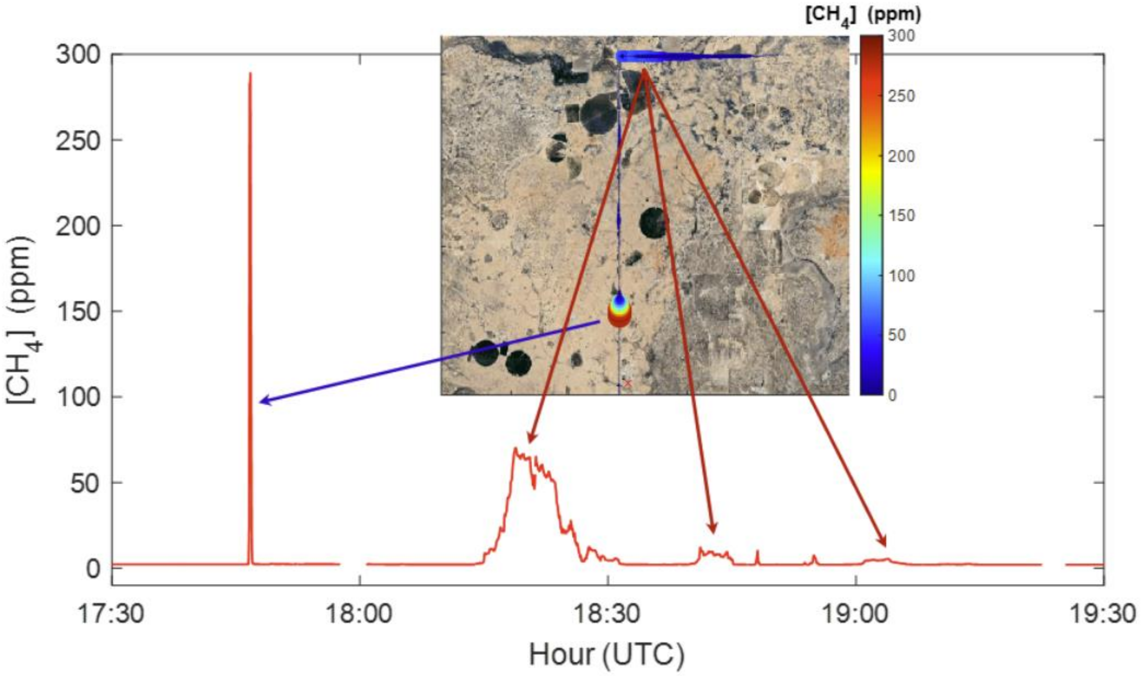

Fig. S9. Time series of methane measured downwind of the eastern release facility during the pipeline blowdown experiment on Oct 8, 2024. The embedded map indicates the observation locations where methane enhancements were detected.

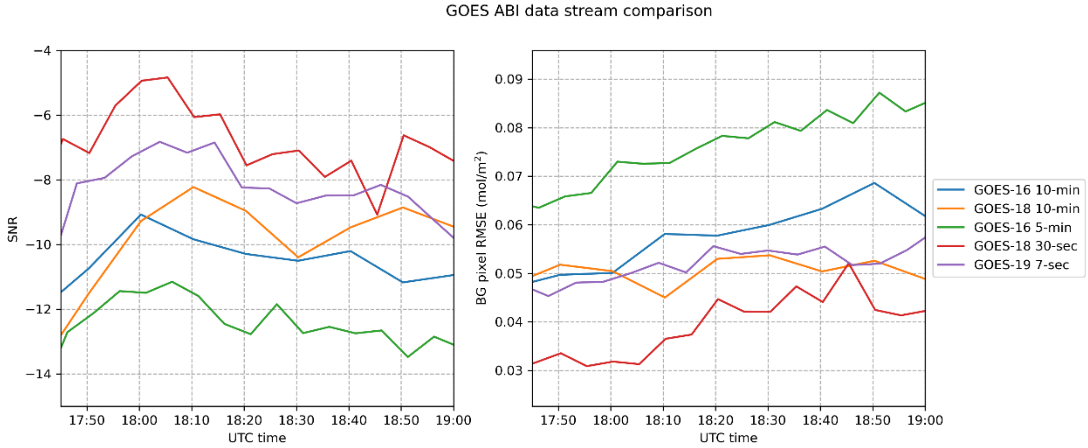

Fig. S10. Time series of signal-to-noise ratio (SNR) and background pixel root mean square error (RMSE) for five GOES ABI data streams during the experiment.

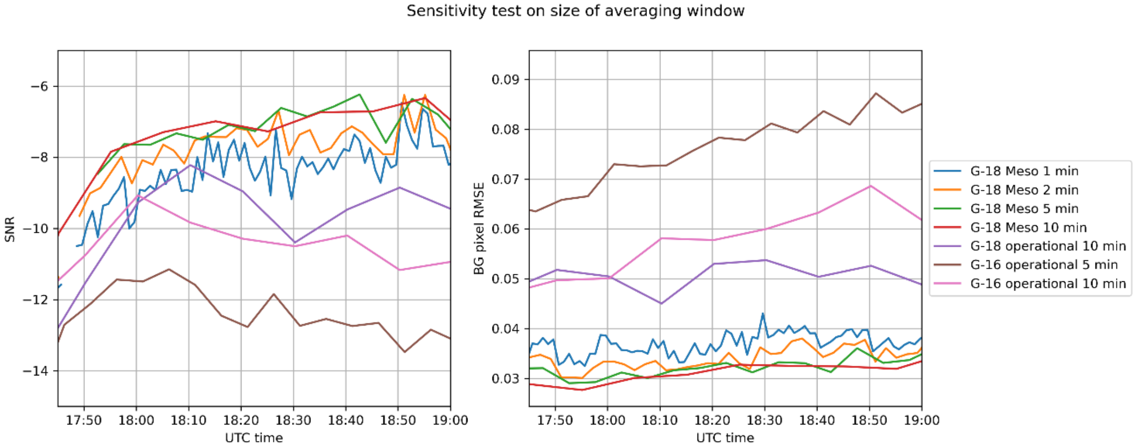

Fig. S11. Time series of SNR and background pixel RMSE for GOES-18 mesoscale imagery smoothed using different window sizes, compared with operational GOES ABI data streams.

Tables

Delays (s)	Ave error (deg)	Ave abs error (deg)	RMSE (deg)	Ave error (deg)	Ave abs error (deg)	RMSE (deg)
0	-23.9	23.9	90.8	-23.0	23.7	167.5
4	-10.3	10.4	45.3	-7.7	12.1	102.1
5	-7.0	8.0	35.7	-3.9	11.1	94.0
6	-3.6	6.8	28.2	-0.1	11.6	91.6
7	-0.2	6.0	24.7	3.6	12.1	94.7

Table S1. Average error, absolute error, and RMSE of wind direction as a function of delay time.

Movie S1 (separate file). Video footage of the methane plumes observed by GOES ABI.

SI References

1. Varon, D. J., Jervis, D., McKeever, J., Spence, I., Gains, D., and Jacob, D. J.: High-frequency monitoring of anomalous methane point sources with multispectral Sentinel-2 satellite observations, Atmos. Meas. Tech., 14, 2771–2785, https://doi.org/10.5194/amt-14-2771-2021, 2021.
2. Clough, M.W. Shephard, E.J. Mlawer, J.S. Delamere, M.J. Iacono, K. Cady-Pereira, S. Boukabara, P.D. Brown, Atmospheric radiative transfer modeling: a summary of the AER codes, Journal of Quantitative Spectroscopy and Radiative Transfer, Volume 91, Issue 2, 2005, Pages 233-244, ISSN 0022-4073, https://doi.org/10.1016/j.jqsrt.2004.05.058.
3. de Jong, T. A., Maasakkers, J. D., Irakulis-Loitxate, I., Randles, C. A., Tol, P., & Aben, I. (2025). Daily global methane super-emitter detection and source identification with sub-daily tracking. Geophysical Research Letters, 52, e2024GL111824. https://doi.org/10.1029/2024GL111824
4. Gerhard Meister, Joseph J. Knuble, Julia A. Barsi, Robert Bousquet, Leland H. Chemerys, Robert E. Eplee, Ulrik Gliese, Samuel Kitchen-McKinley, Shihyan Lee, Jeffrey W. McIntire, Frederick S. Patt, P. Jeremy Werdell, "On-orbit OCI characterization measurements from the first six months of the PACE mission," Proc. SPIE 13192, Sensors, Systems, and Next-Generation Satellites XXVIII, 131920A (20 November 2024); https://doi.org/10.1117/12.3033581
5. Peischl, J., Karion, A., Sweeney, C., Kort, E. A., Smith, M. L., Brandt, A. R., Yeskoo, T., Aikin, K. C., Conley, S. A., Gvakharia, A., Trainer, M., Wolter, S., and Ryerson, T. B. (2016), Quantifying atmospheric methane emissions from oil and natural gas production in the Bakken shale region of North Dakota. J. Geophy. Res. Atmos., 121: 6101-6111. doi: 10.1002/2015JD024631.
6. Peischl, J., Ryerson, T. B., Aikin, K. C., deGouw, J. A., Gilman, J. B., Holloway, J. S., Lerner, B. M., Nadkarni, R., Neuman, J. A., Nowak, J. B., Trainer, M., Warneke, C. and Parrish, D. D. (2015), Quantifying atmospheric methane emissions from the Haynesville, Fayetteville, and northeastern Marcellus shale gas production regions. J. Geophys. Res. Atmos., 120: 2119–2139. doi: 10.1002/2014JD022697.
7. Conley, S. A., I. C. Faloona, D. H. Lenschow, A. Karion, and C. Sweeney, 2014: A Low-Cost System for Measuring Horizontal Winds from Single-Engine Aircraft. J. Atmos. Oceanic Technol., 31, 1312–1320, https://doi.org/10.1175/JTECH-D-13-00143.1.
8. Carroll, B. J., Strobach, E., Baidar, S., Holloway, M. W., McCarty, B., Marchbanks, R., & Brewer, W. A. (2025). Wildfire smoke shading observations: Impacts on boundary layer mixing and thermally driven smoke transport. Journal of Geophysical Research: Atmospheres, 130, e2024JD043303. https://doi.org/10.1029/2024JD043303
9. Tucker, S. C., C. J. Senff, A. M. Weickmann, W. A. Brewer, R. M. Banta, S. P. Sandberg, D. C. Law, and R. M. Hardesty, 2009: Doppler Lidar Estimation of Mixing Height Using Turbulence, Shear, and Aerosol Profiles. J. Atmos. Oceanic Technol., 26, 673–688, https://doi.org/10.1175/2008JTECHA1157.1.